A stronger transcription regulatory circuit of HIV-1C drives the rapid establishment of latency with implications for the direct involvement of Tat

Sutanuka Chakraborty[1*], Manisha Kabi [1,$] and Udaykumar Ranga [1,#]

[1] HIV-AIDS Laboratory, Molecular Biology and Genetics Unit, Jawaharlal Nehru Centre for Advanced Scientific Research, Bangalore, India

Running Title: An enhanced LTR-Tat feedback promotes HIV-1C silencing

Address of correspondence to Prof. Udaykumar Ranga at Molecular Biology and Genetics Unit, Jawaharlal Nehru Centre for Advanced Scientific Research, Jakkur P. O., Bangalore 560064, India. E-mail: **udaykumar@jncasr.ac.in**

[*] Present address: Chemical Engineering Division, CSIR-National Chemical Laboratory, Pune, India

[$] Present address: Genome Architecture, Gene Regulation, Stem Cells and Cancer Programme, Centre for Genomic Regulation (CRG), Barcelona, Spain

Word Count:

Abstract: 150 words

Text: 15395 words

Abstract

The magnitude of transcription factor binding site variation emerging in HIV-1C, especially the addition of NF-κB motifs by sequence duplication, makes the examination of transcriptional silence challenging. How can HIV-1 establish and maintain latency despite having a strong LTR? We constructed panels of sub-genomic reporter viral vectors with varying copy numbers of NF-κB motifs (0 to 4 copies) and examined the profile of latency establishment in Jurkat cells. We found surprisingly that the stronger the viral promoter, the faster the latency establishment. Importantly, at the time of commitment to latency and subsequent points, Tat levels in the cell were not limiting. Using highly sensitive strategies, we demonstrate the presence of Tat in the latent cell, recruited to the latent LTR. Our data allude, for the first time, to Tat establishing a negative feedback loop during the late phases of viral infection, leading to the rapid silencing of the viral promoter.

Importance

Over the past 10-15 years, HIV-1C has been evolving rapidly towards gaining stronger transcriptional activity by sequence duplication of major transcription factor binding sites. The duplication of NF-κB motifs is unique and exclusive for HIV-1C, a property not shared with any of the other eight HIV-1 genetic families. What mechanism(s) does HIV-1C employ to establish and maintain transcriptional silence despite the presence of a strong promoter and a concomitant strong, positive transcriptional feedback is the primary question we attempted to address in the present manuscript. The role Tat plays in latency reversal is well established. Our work with the most common HIV-1 subtype C (HIV-1C) offers crucial leads towards Tat possessing a dual-role in serving both as transcriptional activator and repressor at different

phases of the viral infection of the cell. The leads we offer through the present work have significant implications for HIV-1 cure research.

Introduction

The post-integration HIV-1 latency is characterized by the presence of the transcriptionally silent but replication-competent provirus within the host cells, a challenge for HIV-1 eradication. A significant amount of controversy surrounds HIV-1 latency following the discovery of a latent HIV-1 reservoir in the resting $CD4^{+ve}$ T-cells (1, 2) whether the external host cell parameters or the intrinsic proviral elements are deterministic in modulating HIV-1 latency. While some models consider HIV-1 latency to be an 'epiphenomenon' influenced by the activation status of the host cell and host factors (3-6), others lay emphasis on the stochastic nature of viral gene-expression noise regulated by the LTR-Tat positive feedback circuit, although the influence of the host environmental factors is not disregarded (7-11). Furthermore, several groups have attempted to develop theoretical models to explain the Tat-feedback mediated latency decision in HIV-1 (7, 12).

Master transcriptional regulatory circuits (MTRC) have been identified in prokaryotic and eukaryotic viruses functioning as integral molecular switches to toggle between transcriptional ON and OFF phases. In this context, the lysis-lysogeny decision in bacteriophage λ has been widely researched (13). Fate selection in λ phage is based on the preferential expression of two different key viral proteins, CI and Cro, from a bi-directional promoter, in a mutually exclusive fashion, and on the cooperativity of the CI repressor to establish a 'bistable' circuit manifesting lysis or lysogeny (14). Transcriptional circuits in several latency-establishing eukaryotic viruses function through rate-versus-level trade-off where rapid up-regulation of a viral protein is essential for efficient viral replication, but the

same molecule is cytotoxic at saturating levels. The immediate-early 2 (IE2) transactivator protein of CMV is a typical example of this phenomenon (15-17). The ICP0 and Rta proteins of Epstein Barr virus (EBV) and Herpes Simplex Virus-1 (HSV-1), respectively, exploit the phenomenon of cooperativity to control alternate replication fates (18-22).

Importantly, the transcription regulatory circuit in HIV-1 appears to differ significantly from those of the λ phage or the eukaryotic viruses mentioned above. First, there is no evidence for a repressor molecule or negative feedback loop controlling the HIV-1 circuit while Tat functioning as only an integral component of a positive feedback circuit. Second, the Tat-feedback circuit seems to lack bistability such that Tat transactivates the LTR as a monomer with no self-cooperativity to form multimers (H=1) (23). Tat was proposed to undergo post-translational modifications at specific sites to modulate latency and to account for Tat mono-stability, and the lack of self-cooperativity. It was proposed that enzymatic conversion of acetylated Tat (Tat_A) to a more stable deacetylated form (Tat_D) constitutes a feedback-resistor module with a predominant off state (12). Importantly, the models described above are majorly based on mathematical simulations supported by simple reaction parameters with minimal experimental validation. Of note, these studies exclusively modeled the HIV-1 subtype B system, although other genetic families of HIV-1 contain subtype-specific molecular features.

The examination of transcriptional silence is expected to be technically more challenging in HIV-1C as compared to that in the other subtypes of HIV-1, including HIV-1B, for two different reasons. First, HIV-1C contains several subtype-specific variations in nearly all types of transcription factor binding sites (TFBS) present in the viral promoter, including that of NF-κB, Sp1, RBF-2, and other elements. Among these variations, the copy number

difference of the NF-κB binding elements is the most striking one and unique to HIV-1C. While other subtypes of HIV-1 contain a single (HIV-1E) or two (all others including HIV-1B) NF-κB motifs in the viral enhancer, HIV-1C contains three or four of these motifs (Figure 1). Second, the additional NF-κB binding elements present in HIV-1C are genetically diverse (24). Three different kinds of NF-κB motifs, H, C, and F, may be found in the long-terminal repeat of HIV-1C (C-LTR). We demonstrated previously that the progressive acquisition of the additional NF-κB motifs enhances transcriptional strength of the viral promoter in HIV-1C and confers replication superiority over the canonical viral strains in natural infection, and under experimental conditions (25). Given the positive correlation between the transcriptional strength of the viral promoter and the enhanced strength of transcriptional feedback, it is intriguing how viral latency is favoured in the variant viral strains containing a higher number of NF-κB motifs. In this backdrop, the present study is an attempt to examine the influence of variation in the number of NF-κB binding elements in C-LTR. Of note, the focus of the present study is only on the copy-number difference of the NF-κB binding sites, therefore, on the overall strength of transcription, and its influence on viral latency. The present study does not aim at examining the impact of genetic diversity of NF-κB binding motifs on viral latency.

Using sub-genomic HIV-1C reporter viruses that differed in the LTR-Tat transcriptional feedback architecture and using panels of LTR variant viral strains that varied in the copy-number of NF-κB motifs, we demonstrate for the first time that the enhanced transcriptional strength of the LTR leads to a rapid establishment of viral latency. Further, we explain the apparent paradox by demonstrating that a stronger transcriptional activity of the LTR leads to higher levels of cellular Tat protein, which, above a certain threshold, possibly establishes negative feedback on viral transcription. Importantly, using indirect immunofluorescence and

a highly sensitive proximity ligation assay, for the first time, we demonstrate the presence of Tat in cells harboring an active or a latent provirus. We also show the recruitment of Tat not only to the active but also the latent proviral LTR, albeit at a magnitude several folds lower. Our data, thus collectively allude to Tat playing a deterministic role in initiating transcriptional silence through negative feedback regulation.

RESULTS

The strengths of viral gene expression, as well as Tat-transactivation are directly proportional to the number of functional NF-κB motifs in the HIV-1C enhancer.

The present study is an attempt to examine the influence of variation in the number of NF-κB binding elements in the C-LTR on viral gene expression and latency. To this end, we employed two different Jurkat T cell models, the autonomous Tat-feedback (ATF), and the tunable Tat-feedback (TTF) models to examine HIV-1C latency. The sub-genomic viral vectors encoding EGFP (or d2EGFP, a variant GFP with a shorter half-life), were pseudotyped with VSV-G envelope. The two experimental models differ from each other in the manner the LTR-Tat-feedback axis is regulated. Using these two experimental systems, we examined transcriptional activation and silencing as a function of the promoter strength (by varying the copies of NF-κB motifs ranging from 0 to 4 copies in the ATF model) or the Tat-feedback strength (by modulating the physiological concentration of Tat in the TTF model) or both from a panel of HIV-1C LTRs.

The ‘Autonomous Tat-feedback' (ATF) model of HIV-1 comprises of the presence of only the LTR and Tat, with all the other viral factors being absent, thus retaining the natural functional association between the two major viral factors, as reported previously (7, 26). Several groups have adopted the ATF model to elucidate the mechanisms governing HIV-1

147 latency. In the present study, we modified the pLGIT sub-genomic reporter vector (7) by
148 substituting the Tat ORF and the 3' LTR of the parental vector, both of HIV-1B origin, with
149 the homologs of HIV-1C to construct pcLGIT. In the pcLGIT (cLTR-EGFP-IRES-cTat)
150 vector, the expression of EGFP and C-Tat are under the control of the C-LTR.

151 Given the natural propensity of HIV-1C to contain more copies of the NF-κB motif in the
152 enhancer, three copies typically and up to four copies frequently (24), we constructed a panel
153 of cLGIT viral strains comprising of NF-κB copy-number variant LTRs (p911a series;
154 Materials and Methods). Using the prototype C-LTR containing four functional NF-κB
155 binding sites (FHHC), we introduced inactivating point mutations sequentially into the
156 enhancer to reduce the number of functional NF-κB motifs progressively, from 4 copies to 0
157 copies (Figure 2A). In some of the subsequent experiments involving the ATF model, we also
158 resorted to the cLdGIT panel of viral strains, where the EGFP reporter was substituted with
159 d2EGFP in the pcLdGIT vector backbone with the same set of NF-κB variant LTRs as the
160 pcLGIT (p911b series; Materials and Methods). The viral stocks of the panel pseudotyped
161 with VSV-G envelope were generated in HEK293T cells, and the relative infectious units
162 (RIU) of the stocks were determined in Jurkat cells using EGFP/d2EGFP fluorescence.

163 First, we compared the levels of EGFP expression from the LTR-variant cLGIT panel in the
164 context of a functional, positive Tat-feedback loop, where both the reporter gene and the
165 concomitant Tat-feedback strength are expected to vary based on the autoregulatory circuit.
166 Jurkat cells, infected with each viral strain of the cLGIT panel independently at ~0.5 RIU
167 were either activated with a combination of global T-cell activators (40 ng/ml PMA + 40
168 ng/ml TNFα + 200 nM TSA + 2.5 mM HMBA) or maintained without activation and 24
169 hours following the treatment, both the EGFP fluorescence and the Tat transcript levels were
170 examined using flow cytometry and Tat RT-PCR, respectively (Figure 2B). Representative,
171 stacked histograms depicting the three conditions of treatment - uninfected Jurkat cells (black

dotted histogram), infected but untreated cells (black hollow histogram) and, infected and activated cells (solid grey histogram) corresponding to all the five NF-κB variant strains are presented (Figure 2C). Importantly, when the cell population in each histogram was demarcated into three categories based on the intensity of EGFP expression ($EGFP^{-}$, $EGFP^{Low}$, and $EGFP^{High}$), it was the $EGFP^{High}$ fraction that displayed the most pronounced impact of the NF-κB site copy number difference on transactivation. The percentage of the $EGFP^{High}$ fraction was directly proportional to the number of NF-κB motifs in the LTR, which was also reflected in the peak height of the $EGFP^{High}$ cluster in the stacked histogram profile.

We quantitated EGFP fluorescence in terms of mean fluorescence intensity (MFI) as a function of the copy numbers of NF-κB motifs in the LTR and found a direct proportionality between them (Figure 2D), although the percent of viral infectivity was comparable (inset; Figure 2D). The LTR containing four NF-κB motifs (FHHC; 4-κB) demonstrated the highest fluorescence intensity with (82,917.51 ± 825.7 RFU) and without (12,365.13 ± 179.3 RFU) activation; while, the LTR in which all the four NF-κB motifs have been mutated (OOOO; 0-κB) demonstrated the lowest levels of the reporter expression with (22,190.38 ± 668.1 RFU) and without (6,083.36 ± 290.5 RFU) activation. The activity of the other three LTRs containing 3 (OHHC; 3-κB), 2 (OOHC; 2-κB), or 1 (OOOC; 1-κB) functional NF-κB motifs remained between the two extremes. The fold enhancement in EGFP expression was directly proportional to the number of functional NF-κB motifs in the LTR with a linear correlation ($r = 0.98$) between the transcriptional activity and the functional NF-κB motifs in the LTR (Figure 2E). A viability assay performed using a live/dead stain before the analysis of EGFP expression confirmed minimal cell-death following activation (Figure 2F). Similar to the EGFP MFI profile, the level of Tat transcript expression (Figure 2G) and fold transactivation (Figure 2H) were directly proportional to the number of NF-κB copies in the LTR ($r = 0.96$)

with or without activation. The evaluation of the transcripts of GAPDH, as an internal cellular reference control in a real-time RT-PCR, validated the expression levels of Tat mRNA form the viral panel under diverse cell activation conditions (Figure 2I). It is evident from the expression profile that a perfect correlation exists between the number of NF-κB motifs and the level of gene expression from the promoter. Importantly, the expression of EGFP can be used as a surrogate marker for the expression of Tat, since a perfect correlation exists between the two genes co-expressed from the viral promoter. In the subsequent assays, we routinely used the expression of EGFP as a measure of the transcriptional activity of the viral promoter with frequent confirmation of Tat expression.

A stronger viral promoter establishes latency at a faster rate.

A major paradox in the transcriptional regulation of HIV-1C is that a virus that must establish latency tends to acquire a stronger promoter containing more NF-κB motifs, especially when other genetic families of HIV-1 do not employ such a strategy. To understand this paradox, we used the NF-κB copy number variant strains of the ATF panel to determine the kinetics of latency establishment. Using the experimental strategy depicted (Figure 3A), we infected Jurkat cells at a low RIU (~0.1-0.2) to ensure a single integration event per cell. The cells were allowed to expand before inducing them with a cocktail of global activators, and the $EGFP^{+}$ cells were recovered by sorting. The kinetics of EGFP switch-off was subsequently monitored every four days for 16 days by flow cytometry. A representative strategy of cell gating and sorting is presented (Figure 3B).

Using the experimental strategy described above, and the cLGIT panel of NF-κB copy number variant viral strains containing 4 to 0 copies of the TFBS, we evaluated how the transcriptional strength of HIV-1 LTR would influence the kinetics of latency establishment

over 16 days. The analysis found a profound impact of NF-κB motif copy number on the kinetics of HIV-1 latency establishment. Representative, stacked histogram profiles of the LTR-variant strains depicting the temporal expression pattern of the $EGFP^{+}$ sorted cells are presented (Figure 3C). Although latency establishment was evident for all the five LTRs examined, the rapidity of latency establishment unexpectedly was directly proportional to the number of NF-κB motifs in the viral enhancer (Figures 3D and 3E). In other words, the stronger was the transcriptional activity of the LTR, the faster the latency was established. Based on the slope of EGFP downregulation, the LTRs could be classified into two broader groups: The two strong promoters, the 3- and 4-κB LTRs, down-regulated the EGFP expression at a significantly faster rate than the other three not strong promoters 2-, 1- and 0-κB LTRs. In the present manuscript, we classify the LTRs into two groups, 'strong' and 'weak' based on the difference in the transcriptional strength, a categorization consistent with many other properties we analyzed subsequently, although the 2-κB LTR occasionally occupied an intermediate position (see below). For instance, the EGFP intensity values (RFU) of 4-κB LTR reduced approximately 8-fold from a value of 30,631.64 ± 1,278.3 on D0 to 3,771.06 ± 245.2 on D16, whereas the corresponding values for the weakest 0-κB LTR were the modest and reduced by only two-folds during the same period from 4,455.11 ± 258.9 to 2,371.98 ± 59.3. Of note, although both 3- and 4-κB LTRs demonstrated a rapid EGFP downregulation, the 3-κB LTR established viral latency at a faster rate, and the difference between the two promoters was highly reproducible and significant. It is not clear if this difference may have implications for the relative replication fitness of the two viral strains.

The expression profile of the Tat transcripts determined using an RT-PCR on days 0, 8 and, 16 also correlated directly with the NF-κB copy number in the LTR, as expected (Figure 3H) and resembled that of the EGFP MFI profile of the LTRs. A profound reduction in Tat expression was observed for all the viral promoters between days 0 and 8. The 4-κB LTR

showed the highest level of Tat expression, 92.94 ± 5.4 at D0 that dropped to 12.02 ± 0.8 at D8 and subsequently to 2.3 ± 0.01 at D16. The corresponding values for the 3-κB LTR are 71.76 ± 2.5, 12.8 ± 0.73, and 1.15 ± 0.1, respectively. Of note, comparable expression of GAPDH transcripts was observed from the viral panel at all the time points of latency establishment as quantitated using a real-time PCR (Figure 3I). Furthermore, using a Taqman qPCR, we confirmed a single integration event per cell in all the five stable cell pools, thus ruling out the possibility that the difference in the integration frequency influenced the outcome of the analyses (Figure 3J). A live/dead exclusion assay indicated a comparable percentage of live cells among the panel members, and uniform cell viability was maintained temporally throughout latency establishment (Figure 3K). Importantly, the live/dead gating excluded the dead cells before the EGFP analysis (post-sort gating; Figure 3B); thus, precluding the possibility of EGFP auto-fluorescence from dead cells influencing the data analysis. In summary, our data are suggestive that the enhanced strength of HIV-1C LTR due to the increase in the number of NF-κB sites could play a decisive role in regulating viral latency. A positive correlation between the Tat-transcript levels and the rapid rate of EGFP switch-off by the strong viral promoters is strongly indicative of the Tat-mediated positive feedback loop playing a critical role in establishing viral latency.

The kinetics of latency establishment is predominantly a function of the EGFP^{High} cells displaying a biphasic mode of transcriptional silence.

At the baseline of the above assay, all the variant viral strains were represented by nearly 100% EGFP^{+} cells, but with a varying range of EGFP fluorescence intensities (referred to as total EGFP^{+} cells throughout the manuscript). However, a marked difference in the mean intensity of EGFP among the LTR-variants was noted at D0 time point post-sorting (compare

Figures 3D and 3E). This apparent paradox could be explained by analyzing only the EGFP^{High} cells but not the total EGFP^{+} population. In the present essay, we, therefore, gated the cells into two additional subpopulations - EGFP^{High} (MFI >10^4 RFU) and EGFP^{Low} (MFI ~10^2-10^4 RFU) - as depicted in the post-sort gating strategy (Figure 3B), as evident in the histogram profile of each NF-κB variant strain (Figure 3C). Kinetic curves of % EGFP^{High} and EGFP^{Low} cells were then constructed from the above-gated subpopulations. Importantly, the reduction in the total EGFP MFI (Figure 3D) as well as the Tat-transcript levels (Figure 3H) corresponded perfectly only with the % EGFP^{High} cells (Figure 3F), but not with the % EGFP^{Low} cells (Figure 3G). Thus, the EGFP^{High} cells, not the total EGFP^{+} cells, are decisive in regulating viral latency. Additionally, the % EGFP^{High} temporal curves of the strong (3- and 4-κB) versus weak LTRs (0-, 1- and even 2-κB) were profoundly different. Firstly, on day 0, the strong LTRs produced the highest percentage of EGFP^{High} cells as compared to the weak LTRs. Secondly, the latency establishment of the strong LTRs appeared to have manifested in two distinct phases: a rapid reduction of EGFP expression between days 0 and 8 and a slower rate of decrease after D8; the bi-phase latency profile was either absent or not prominent with the weak LTRs. Thirdly, the rapid fall in EGFP expression of the EGFP^{High} pool of the strong LTRs between days 0 and 8 synchronized with a significant rise in the EGFP^{Low} cell pool peaking on D8. These data collectively allude to the critical role the transcriptional strength of HIV-1 LTR plays in latency establishment. In summary, the EGFP^{High} cell pool, not that of the EGFP^{Low} cells, plays a decisive role in the population latency kinetics of the virus.

LTR-silencing in the GFP^{High} cells implicates Tat feedback

Given the apparent significance of the EGFP^{High} phenotype for HIV-1 latency establishment, we investigated the phenomenon further by sorting only the EGFP^{High} cell pools for all the

NF-κB variant strains that represented a population with a comparable level of fluorescence intensity (Figure 4). At Day 0, the EGFP MFI values were uniform among the variant viral strains of the panel and we monitored downregulation of the green fluorescence every four days for 24 days (Figure 4A). A clear distinction between the strong (4- and 3-κB) and the weak (2-, 1-, and 0-κB) LTRs was evident in the EGFP MFI profile (Figure 4B) or when the $EGFP^{+}$ percentage was considered (Figure 4C), although the 2-κB LTR sometimes occupied an intermediary position; the rate of latency establishment was significantly rapid for strong LTRs. The biphasic mode of latency establishment, rather than a gradual and monophasic mode, was evident from the stacked histogram profiles of the sorted $EGFP^{High}$ pool (Figure 4F). We demonstrated above that a progressively increasing NF-κB site number in the LTR steadily enhances the transcriptional strength as well as the physiological concentration of Tat (Figures 2D and 2G). We, therefore, speculate that higher cellular Tat levels, an invariable outcome of the stronger positive transcriptional feedback, are necessary for the rapid silencing of the LTR as manifested by the $EGFP^{High}$ cells of the strong LTRs.

Of note, the process of latency establishment above was not complete with any of the LTRs of the cLGIT panel, regardless of the transcriptional strength. The percent of $EGFP^{+}$ cells reached only the halfway mark after 24 days of sorting even for the strong LTRs that established latency at a faster rate (Figures 4B and 4C). Importantly, the long half-life of the EGFP, ~ 48 h, used in these vectors as a surrogate marker for latency did not represent the actual dynamics of the LTR transcriptional activity faithfully. The cells were continued to be scored as positive for EGFP fluorescence for a significant period even after the LTR was switched off, leading to a false positive scoring. To rectify this problem, we substituted EGFP in the reporter viral strains with d2EGFP characterized by a significantly shorter half-life (2

vs. 48 h) (27). The viral strains of the new panel (cLdGIT) are analogous to the previous panel.

Using the new panel, we sorted the d2EGFP^{High} cells as above to establish the profiles of latency. Several differences in the profiles of latency were readily evident between the cLGIT and cLdGIT panels (compare Figures 4B and 4D; 4C and 4E). Unlike the cLGIT panel, the cLdGIT variants successfully established a near-complete viral latency, and all the members of the panel demonstrated latency establishment at a faster rate; the d2EGFP MFI values reduced to the baseline within 96 h following sorting (Figure 4D). Although the substitution of EGFP with d2EGFP masked the differences in latency kinetics among the members of the cLdGIT panel to some extent, the overall pattern of latency establishment was consistent with that of the cLGIT counterparts. The percentage of the cells downregulating d2EGFP expression was directly proportional to the number of the NF-κB motifs in the viral promoter (Figure 4E). For instance, the time required for the loss of fluorescence in half of the cells (FL_{50}) was estimated to be 23.3, 22.1, 24.64, 32.9, and 48 h for the 4-, 3-, 2-, 1-, and 0-κB viral strains, respectively. Thus, a direct correlation between the transcriptional strength of the viral promoter and the rate of latency establishment was consistent between the cLdGIT and cLGIT panels. The bi-phasic mode of latency establishment was also evident in the cLdGIT model (Figure 4G).

Collectively, our data are assertive that the transcriptional strength of the HIV-1 promoter is an essential regulatory parameter for viral latency. Further, the latency kinetics in the Tat-transactivated population (GFP^{High} cells), of two different models, cLGIT and cLdGIT vectors of the ATF panel, followed an NF-κB-site copy number-dependent transcriptional silencing.

A bimodal (ON or OFF) latency establishment in the pools of cloned cell lines

The observation that the transcriptional strength of the LTR and the feedback loop of Tat function synergistically to silence the viral promoter was drawn based on cell pools. Since individual cells in a pool are heterogeneous in several biological properties, including the site of proviral integration, we examined the nature of the latency profile in multiple cloned cell lines of all the five LTR variants. Jurkat cells were infected with the viral strains of cLGIT (ATF) panel, stimulated with the global activation cocktail, single $EGFP^{High}$ cells were sorted into individual wells of a 96-well culture plate, the sorted cells were allowed to expand for 3-4 weeks, and the EGFP expression profiles were assessed by flow cytometry (Figure 5A). We recovered 16-25 clones from each NF-κB variant, and 16 clones from each variant were randomly selected for the latency analysis. Of note, since each cell line descended from a single parental cell, all the daughter cells derived from the parental cell are expected to have a common site of integration.

Based on the EGFP expression pattern, the clones could be categorized into three distinct types (Figure 5B). The persisters, all the daughter cells descending from a single parental cell sustain expression of high-intensity EGFP throughout the observation period of 28 days and even beyond, comparable to that of the original parental cell, indicative of a provirus transcribing actively in all the daughter cells. The relaxers, all the daughter cells of the $EGFP^{High}$ parental cell, have switched-off EGFP expression entirely during the period of observation. The bimodallers, the third clonal type, demonstrated a distinctive feature of the simultaneous existence of both the phenotypes among the daughter cells, although all the cells in the cluster were derived from the same $EGFP^{High}$ parental cell. One subset of the cells maintained high EGFP expression ($EGFP^{High}$), whereas the other subset down-regulated the

368 reporter gene completely ($EGFP^-$) with the minimal manifestation of an intermediate
369 phenotype.

370 Importantly, all the five viral strains of the panel displayed the three clonal phenotypes
371 described above with the distinction that the proportion of the three phenotypes is directly
372 correlated with the copy number of NF-κB sites in the LTR. Given the limitation of available
373 cells for the flow analysis, we could determine the phenotype of the clonal cells only at D21
374 and D28, not earlier. We analyzed 16 randomly selected clones for each of the five LTRs of
375 the panel (Figure 5C). The profile of the three phenotypes varied significantly among the
376 members of the panel and appeared to associate with the transcriptional strength of the LTR.
377 On D21, a larger proportion of cell lines representing the strong viral promoters (4- and 3-κB
378 LTRs) transited to the OFF state as compared to those of weak promoters (1- and 0-κB
379 LTRs); in contrast, the cells of 2-κB LTR occupied an intermediate position. On D28, the
380 strong LTRs contained no persistent phenotype and fewer bimodal clones. The strong viral
381 promoters downregulated EGFP expression, both persistent and bimodal phenotypes at a
382 significantly faster rate as compared to the other three promoter variants. Despite the
383 limitation of the small number of clonal cell lines used in the analysis, these data are broadly
384 consistent with the results of cell pools (Figure 4). Thus, cell pools and clonal cell
385 populations, both the models demonstrated a direct correlation between the transcriptional
386 strength of the LTR and the rate of latency establishment. Further, both the experimental
387 models are also consistent with each other in demonstrating a bimodal, not a gradual, latency
388 establishment.

389 The clonal cell lines that display the bimodal EGFP phenotype offer an excellent
390 experimental model as these clonal lines demonstrate two contrasting phenotypes ($EGFP^{High}$
391 and $EGFP^-$ expression) despite an identical viral genotype, chromatin background and, host-
392 cell activation. We selected two clones, 3c and 8c representing the strong 4-κB and 3-κB

393 LTRs, respectively, and characterized them for their bimodality. The two daughter
394 populations, $EGFP^{High}$ and the $EGFP^{-}$ were subsequently enriched using FACS sorting and
395 examined for the nature of transcription complexes recruited to the active and silent LTRs
396 using ChIP analyses (see below). Importantly, a vast majority of the $EGFP^{-}$ cells of the
397 bimodal clones representing the 4- or 3-κB LTRs could be fully reactivated to the $EGFP^{High}$
398 phenotype; 95.6% (Figure 5D) and 90.4% (Figure 5H) $EGFP^{High}$ cells, respectively,
399 following global activation. The levels of proviral integration between the two
400 subpopulations of each bimodal clone were comparable and close to ~1.0 (Figures 5E and
401 5I), ruling out the possibility of integration frequency differences underlying the bimodal
402 phenotype. Importantly, the Tat transcript levels in the $EGFP^{+}$ subfractions of both the clonal
403 cell lines were significantly higher compared to their $EGFP^{-}$ counterparts, approximately 112
404 folds for the 4-κB (Figure 5F) and 80 folds for the 3-κB clones (Figure 5J). We also excluded
405 the possibility of the bimodal phenotype arising from cell cycle differences between the two
406 phenotypes. We compared the proportion of cells in the different phases of the cell cycle (G1,
407 S, and G2/M) between the $EGFP^{-}$ and $EGFP^{High}$ subpopulations. We found that the cell
408 proportions were comparable in both the phenotypes. The data were reproducible in both the
409 4- (Figure 5G) and the 3-κB (Figure 5K) clones; the manifestation of the two contrasting
410 phenotypes in the bimodallers was therefore unlikely to be a consequence of cell-cycle
411 differences.

412

413 **A tunable regulatory circuit of HIV-1 transcription alludes to the direct role of Tat in**
414 **latency establishment**

415 The stronger transcriptional activity of the LTR is expected to lead to a proportionately
416 higher expression of Tat, which in turn should increase the transcriptional activity of the LTR
417 further. As a consequence of the unique arrangement, the two principal regulatory elements

418 collectively modulate viral gene expression. In this backdrop, the profile of latency kinetics
419 observed using the ATF model above cannot be ascribed to the different functional activity of
420 either of the elements alone. It was, therefore, necessary to employ a strategy where Tat
421 transactivation alone becomes a variable factor while the transcriptional strength of the LTR
422 remains constant. To this end, we constructed a new HIV-1-Jurkat cell line model, the
423 'Tunable Tat-feedback' (TTF) model, where the transactivation strength of Tat can be
424 modulated independently while keeping the transcriptional strength of the LTR constant. Tat
425 in the TTF model was engineered to possess two unique properties as compared to that in the
426 ATF model (Figure 6A). First, Tat was fused with DsRed2-RFP (stated as RFP throughout
427 the manuscript) to express as a fusion protein enabling the direct visualization of its
428 expression. The new HIV-1 reporter vector pcLdGITRD (cLTR-d2EGFP-IRES-
429 Tat:RFP:DD), thus, co-expressed two different fluorescent proteins, d2EGFP and Tat-RFP,
430 under the control of the LTR. Second, the Tat-RFP fusion protein was tagged with the C-
431 terminal degradation domain (DD) of FK506 binding protein (Tat:RFP:DD). The DD domain
432 can target the fusion protein for rapid proteasome-mediated degradation (28). Shield1, a small
433 molecule ligand, however, can rescue the DD-mediated degradation by specifically
434 interacting with the DD motif and stabilizing the target protein in a dose-responsive manner
435 (29). The sub-genomic HIV-1 reporter vector pcLdGITRD, representing the TTF model,
436 thus, can fine-tune the intracellular concentration of the 'Tat:RFP:DD' fusion protein by
437 changing the concentration of Shield1 in the culture medium, in the context of a fixed LTR
438 strength.
439
440 We constructed a panel (cLdGITRD, the p913 series; Materials and Methods) of two LTR-
441 variant viral strains consisting of 3 or 1 NF-κB motifs, representing the strong and weak
442 LTRs, respectively (Figure 6A). A direct correlation between the Shield1 concentration in the

443 medium, ranging from 0 to 5 μM, and the intensity of Tat-RFP expression was observed in
444 HEK293T cells using the 3-κB viral reporter vector (Figure 6B). Importantly, the viruses
445 could infect the target Jurkat cells. We evaluated the levels of d2EGFP expression and the
446 Tat-mediated transactivation, with an increasing concentration of Shield1 in the medium,
447 using the experimental strategy as depicted (Figure 6C). Interestingly, the effect of Shield1
448 concentration was directly manifested on the d2EGFP^{High} population in the stacked histogram
449 profile (black arrow), indicating Shield1 dose-dependent Tat transactivation and also
450 confirming that the d2EGFP^{High} phenotype represented the Tat-transactivated cells (Figure
451 6D). A direct correlation was also established in the stable Jurkat cells between the Shield1
452 concentration and d2EGFP MFI or 'Tat:RFP:DD' expression (Figures 6E and 6H
453 respectively) suggesting Shield1-dependent stabilization of the 'Tat:RFP:DD' cassette and
454 the subsequent Tat-mediated LTR transactivation. Of note, although we normalized the viral
455 infection, the % d2EGFP^{+} values demonstrated a dose-response proportional to the Shield1
456 concentration even though the d2EGFP itself does not contain the DD of FKBP (Figure 6G).
457 The optimal fold activation of the d2EGFP expression (Figure 6F) and Tat transcript levels
458 (Figure 6I) were found to be 1 μM and 2.5 μM, respectively. In the subsequent experiments,
459 therefore, we used Shield1 in the range of 0 to 3 μM.
460
461 Importantly, the fusion of Tat with DsRed2-RFP offered the advantage of tracking the
462 expression of Tat in real-time during latency establishment. To determine the kinetics of
463 latency establishment in Jurkat cells, we used an experimental schematic as depicted (Figure
464 7A). Jurkat cells were infected with 3- or 1-κB viral strain at an RIU of ~0.1-0.2 in the
465 presence of 1 μM Shield1 and expanded for a week in the presence of Shield1. Subsequently,
466 the cells were activated with the global activators for 24 h, the d2EGFP^{High} population (MFI
467 ~10^4 RFU) was sorted, the sorted cells were maintained separately at four different

concentrations of Shield1 (0, 0.5, 1.0 and 3.0 μM), and the levels of d2EGFP and Tat-RFP expression were monitored every 24 h by flow cytometry.

The TTF model of latency offered several essential insights. Importantly, the ability to visualize two different fluorescent proteins (d2EGFP and Tat:RFP:DD) co-expressed under the LTR permitted to identify the different stages of the viral gene expression and latency, which we collectively refer to as the viral 'latency cycle'. Although both the fluorescent proteins were expressed under the control of the same viral promoter, the expression of d2EGFP was perceptible earlier and at a higher intensity than that of the Tat:RFP:DD fusion protein. The increased molecular size of the Tat:RFP:DD fusion protein, the slow maturation of DsRed2, and the compromised translation efficiency due to the IRES element, all may have contributed to the observed difference between the d2EGFP and Tat-RFP expression profile (Figure 7B, Day 0). The profile of gene expression through the different phases of the latency cycle is remarkably different between the two viral promoters. The transiting of the cells through the successive phases of the latency cycle is illustrated explicitly when the 3-κB LTR profile is examined (Figure 7B, top panel). At Day 0 following the d2EGFP^{High} sort, the vast majority of cells (92.8%) were d2EGFP^{+} Tat-RFP^{-} representing a transcriptionally active viral promoter (Figures 7B, top panel; Day 0 and 7C). During the following 24 hours, the d2EGFP^{+} Tat-RFP^{-} cells exited this compartment via two distinct and diagonally opposite routes. While a significant proportion of these cells (approximately 15%) switched off d2EGFP expression to directly return to the d2EGFP^{-} Tat-RFP^{-} compartment, approximately 6.6% of cells up-regulated Tat-RFP expression from the 3-κB LTR to transit to the d2EGFP^{+} Tat-RFP^{+} compartment alluding to a strong Tat-dependent transcriptional activity (Figures 7B, top panel; Day 1 and 7D). At the subsequent time points, d2EGFP^{+} Tat-RFP^{-} cells continued to vacate this compartment using both the exit routes to reach the d2EGFP^{-} Tat-

493 RFP$^-$ compartment such that on Day 6, 84.3% of the viral strains re-established latency under
494 the strong viral promoter. Importantly, the cells in the d2EGFP$^+$ RFP$^+$ compartment, unlike
495 those of the d2GFP$^+$ Tat-RFP$^-$ compartment, appeared to move to latency only in one
496 direction to the d2EGFP$^-$ Tat-RFP$^+$ compartment (Figures 7B, top panel; Day 3 and 7E). The
497 relative proportion of the cells present in the d2EGFP$^-$ Tat-RFP$^+$ compartment was
498 significantly higher than that of the d2EGFP$^+$ Tat-RFP$^+$ compartment at time points after Day
499 1 alluding to the unidirectional movement of these cells to latency. Importantly, the d2EGFP$^-$
500 Tat-RFP$^+$ compartment is unique since this quadrant represents the proviruses that have
501 'recently' switched off transcription, with significant levels of physiological Tat still
502 persistent in the system as indicated by the RFP$^+$ phenotype. The proviruses of the d2EGFP$^-$
503 Tat-RFP$^+$ compartment also transited to latency only in one direction and entered d2EGFP$^-$
504 Tat-RFP$^-$ compartment (Figure 7B, top panel; Day 5 and 7F).
505
506 In contrast, the 1-κB LTR predominantly displayed the Tat-independent transactivation
507 (Figure 7B, bottom panel). Although approximately 4% of these cells expressed Tat-RFP at a
508 Shield1 concentration of 3 μM, the Tat-RFP expression was delayed by 24 h, as compared to
509 that of the 3-κB LTR, with the Tat-RFP expression reaching a peak only on D3. Importantly,
510 despite the presence of Tat, these dual-positive cells of 1-κB LTR (d2EGFP$^+$ Tat-RFP$^+$) did
511 not move forward to the d2EGFP$^-$ Tat-RFP$^+$ compartment, unlike those of 3-κB LTR, but
512 returned to the d2EGFP$^+$ Tat-RFP$^-$ quadrant (Figure 7B, bottom panel; Day 3). The proviruses
513 activated by Tat-independent transactivation primarily manifested the d2EGFP$^+$ Tat-RFP$^-$
514 phenotype, and these viruses returned to latency by switching off the d2EGFP expression and
515 typically not inducing Tat-RFP expression. While a large majority of 3-κB LTR viral strains
516 and nearly all the viral strains of 1-κB LTR followed this route of latency, a smaller
517 proportion of proviruses of 3-κB LTR moved forward activated by Tat-dependent

518 transactivation that manifested the d2EGFP^{+} Tat-RFP^{+} phenotype. Approximately 14% of the
519 3-κB LTR viral strains were activated by the Tat-dependent transactivation that followed a
520 unidirectional trajectory to latency via the d2EGFP^{+} Tat-RFP^{+} and d2GFP^{-} Tat-RFP^{+}
521 compartments. In contrast, approximately, only 1% of 1-κB LTR viral strains could follow
522 the Tat-dependent transactivation, while the reminder induced only by the Tat-independent
523 activation and returning to latency directly from the d2EGFP^{+} Tat-RFP^{-} compartment. Thus,
524 the transcriptional strength of the viral promoter appears to play a critical role in not only
525 regulating the activation of viral gene expression but also the latency kinetics and whether or
526 not Tat-dependent transactivation is recruited to the LTR. Only the strong 3-κB LTR, but not
527 the weak 1-κB LTR, could successfully undergo Tat-dependent transactivation. The major
528 routes of entry into latency (Tat-dependent or Tat-independent) exhibited by the two LTR
529 variants are shown in solid-black arrows, while their less dominant trajectories are indicated
530 in dotted-black arrows in Figure 7B. Individual trajectories of the percentages of the four
531 distinct fluorescent populations are presented (Figures 7C, 7D, 7E, and 7F).
532
533 Interestingly, a clear demarcation in the profiles of the weak and strong LTRs is evident at
534 the level of the Tat-independent transactivation – in the Tat-RFP negative cell populations
535 (Figures 7C and 7F). The d2EGFP^{+} Tat-RFP^{-} cells of the 3-κB LTR down-regulated d2EGFP
536 at all the concentrations of Shield1 by D4. In contrast, latency establishment in the same
537 population of the 1-κB LTR was incomplete, and nearly half of these cells remained
538 d2EGFP^{+} on D6. This was primarily because a subset of the d2EGFP^{+} Tat-RFP^{-} cells at the
539 later time points (D1 and beyond) followed the Tat-dependent route to latency in the case of
540 the strong 3-κB, but not the weak 1-κB promoter. Therefore, from the data of the TTF model,
541 it appears that Tat-dependent transactivation can silence the promoter at a faster rate as
542 compared to that of the Tat-independent pathway. Further, the kinetics of percent d2EGFP^{+}

to d2EGFP^{-} transition, irrespective of the Tat-RFP expression, demonstrated an identical pattern of promoter silencing in the TTF model with the strong promoter (3-κB) facilitating a faster rate of silencing compared to the weak promoter (1-κB) when compared with the ATF model (3- and 4- κB vs. 2-, 1- and 0-κB LTRs). At all the concentrations of Shield1, the strong 3-κB LTR switched off faster than the weak 1-κB LTR. Thus, the data obtained from the TTF model are strongly suggestive that the transcriptional strength of the HIV-1 LTR plays a critical role in controlling viral latency as a validation of the ATF model. A strong LTR is not only faster in establishing viral latency but also is rapid in revival kinetics from latency, whereas a weak viral promoter appears to be restricted in both the functions.

A sustained presence of Tat in the nucleus following the LTR switch-off

The latency kinetics of two different cellular models (ATF and TTF) alluded to the direct involvement of Tat in the transcriptional suppression of the viral promoter, in a concentration-dependent manner. Furthermore, we could detect the presence of Tat-RFP fusion protein in cells harboring a transcriptionally silent provirus (d2EGFP^{-} Tat-RFP^{+}) containing a strong viral promoter (3-κB-LTR) (Figure 7). Therefore, it was necessary to evaluate the physiological levels and the relative distribution of Tat in cells concomitant with LTR-silencing. To this end, we tracked the expression pattern of the Tat protein in Jurkat cells using indirect immunofluorescence while the cells transited from the 'ON' to the 'OFF' state. Jurkat cells infected with the J-cLdGIT-3-κB viral strain encoding d2EGFP (ATF model) were monitored at 4 - day intervals up to day 16 for d2EGFP expression using flow cytometry (Figure 8A, left panel). At Day 0, the d2EGFP^{High} cells were sorted and subjected to indirect immunofluorescence for Tat at different points (D0, D4, D8, D12, D14, and D16)

(Figure 8A, right panel). A combination of a high-titer, polyclonal, rabbit anti-Tat primary antibody, and an anti-rabbit, Alexa-568 conjugated secondary antibody was used in the assay.

d2EGFP expression analysis by flow cytometry found a progressive downregulation of the fluorescence, and by D8 and D16, only 6.9% and 1% of the cells, respectively, remained positive. The profile of d2EGFP expression of individual cells captured by confocal microscopy was perfectly consistent with that of the flow analysis; and, visible fluorescence could not be detected at D8 and beyond. However, trace levels of Tat expression as determined by the indirect immunofluorescence of Tat (Tat-Alexa 568 signal) could be visually noted above the background on D12 and D16 despite the complete downregulation of d2EGFP, indicating the sustained presence of Tat in an LTR-OFF context. Of note, Tat expression was found in two different compartments of the cells, nuclear and extra-nuclear, the latter mostly localized to the cell membrane. Fluorescent intensities of d2EGFP expression, as well as that of Tat-Alexa 568, were determined independently in the nuclear and the extra-nuclear compartments of 150 individual cells, at all the time points (Figure 8B). The threshold levels of fluorescent protein expression were determined by using uninfected Jurkat cell control for d2EGFP (Lane-8; n = 10) and no-primary antibody control for Tat (Lane-6; n = 10). Importantly, while the fluorescence of d2EGFP reduced progressively with time and fell below the threshold by D12 representing the establishment of latency, the fluorescence of Tat, in either compartment, did not drop below the Tat-Alexa 568 threshold even at D16. The slopes of reduction of the Tat intensities during the initial phases (D0 to D4) of latency-establishment were estimated to be -74.54 ± 16.8 and -37.28 ± 3.2 in the extra-nuclear and nuclear compartments, respectively. At the later time points (D8, D12, and D16), there was only a moderate reduction in the Tat levels in either of the compartments. The data are thus suggestive of a higher level of stability of Tat in the nucleus with possible

591 implications for HIV latency. Importantly, the data of Tat-immunofluorescence are in perfect
592 agreement with the results of the TTF model, where the few d2EGFP^{-} Tat-RFP^{+} cells at the
593 later stages of promoter-silencing indicated sustained presence of low-levels of Tat molecules
594 in the LTR-switched OFF cells (Figure 7B; top panel). In summary, immunofluorescence not
595 only detected the presence of Tat in the latently infected cells as late as D16 post-sorting but
596 also demonstrated a rapid loss of Tat from the extra-nuclear compartment while its relative
597 stability in the nucleus.

598

599 **The in situ proximity ligation assay (PLA) detects the presence of Tat in the latently**
600 **infected cells.**

601 In indirect immunofluorescence, the over-all intensity of the Tat at D12, D14, and D16 in
602 both the cellular compartments was only marginally above the background level. To increase
603 the sensitivity and detect limited quantities of Tat in the 'LTR OFF' cells, we used the highly
604 sensitive proximity ligation assay (PLA), which conjugates immunostaining with the rolling-
605 circle replication and outperforms the traditional immune assays in sensitivity to detect trace
606 amounts of endogenous proteins (30, 31). We optimized Tat-PLA in HEK293T cells using a
607 pair of anti-Tat primary antibodies raised in different hosts (rabbit and mouse). Since PLA
608 does not work well in non-adherent cells, and our attempts to adapt the protocol to the Jurkat
609 cells were not successful, we used HEK293/HEK293T cells in this assay. Using sub-genomic
610 viral vectors encoding Tat representing HIV-1B (pLGIT) or HIV-1C (pcLGIT), we optimized
611 PLA (Figures 9A and 9B). The B-Tat protein could be detected as distinct white dots as
612 opposed to sparse dots in no-antibody and single antibody controls (Figure 9A). Moreover, a
613 dose-response in the intensity of PLA dots and plasmid concentration, as well as a good

614 correlation between the PLA dot number and GFP MFI, are evident in the case C-Tat (Figure
615 9B).

616 Using the optimized PLA protocol for Tat, we asked if the Tat protein could be detected in
617 d2EGFP OFF cells. To this end, HEK293 cells stably and independently infected with the 4-
618 and the 3-κB variants of the ATF-cLdGIT panel were sorted for the d2EGFP^{High} cells. After a
619 week of incubation following the enrichment, approximately 50% of the cells expressed
620 d2EGFP, and the cell pool contained both active (d2EGFP^{+}) and latent (d2EGFP^{-}) cell
621 clusters. Tat-PLA was then performed using the mixed d2EGFP pool corresponding to both
622 the strong LTR (3- and 4-κB) variants to quantitate the Tat-PLA signals in the alternate
623 phenotypes (active and latent). The cells stained with either of the antibodies alone did not
624 show any Tat-specific signals confirming the specificity of the assay (Figure 9C left panel,
625 top two lanes). Tat-specific staining was evident only in the presence of both the antibodies
626 not only in the d2EGFP^{+} cells but also in the d2EGFP^{-} cells (Figure 9C left panel; bottom two
627 lanes). The average number of Tat-PLA dots per cell was determined in a total of 164
628 d2GFP^{+} cells (128 and 36 cells for 4-κB and 3-κB variants, respectively) and 168 d2EGFP^{-}
629 cells (123 and 45 cells for 4-κB and 3-κB variants, respectively) comprising of three
630 independent experiments (Figure 9C; right panel). These values were found to be 3.35 ± 0.77
631 and 2.8 ± 0.59 for d2EGFP^{+} and d2EGFP^{-} cells, respectively, although the difference was not
632 significant statistically. The Tat-PLA data in HEK293 cells confirmed the presence of Tat in
633 the latent cells at a concentration comparable to that of active viral transcription.

634

635 **Differential occupancy of cellular complexes on active and silent LTRs of bimodal**
636 **clones.**

637 Burnett JC et al. examined the differential occupancy of NF-κB factors (p50 and p65) at each
638 of the two identical NF-κB motifs (I and II) in HIV-1B LTR by introducing inactivation
639 mutations into each of these sites individually and the corresponding impact on the
640 transcriptional activity (26). A similar examination at the C-LTR has not been performed. A
641 previous report from our laboratory demonstrated that NFAT1 and 2 proteins could be
642 recruited to the C-κB motif, the variant NF-κB motif unique for HIV-1C, with an affinity
643 superior to that of the canonical H-κB site (32). We attempted to compare the identity of the
644 transcription factors and other host factors binding to the viral promoter between the active
645 and suppressed states under identical experimental conditions.

646 Having demonstrated the presence of Tat in the cells containing the latent provirus in both the
647 TTF (Figure 7), and ATF (Figures 8 and 9) models by flow cytometry and confocal imaging,
648 respectively, we, next asked if Tat in these cells is recruited to the latent viral promoter. We
649 sorted the d2EGFP^{High} and d2EGFP^{-} cell populations from the two clonal cell populations and
650 using the chromatin immunoprecipitation assay, we examined for the presence of several
651 essential host factors or epigenetic marks (Rel family members- p50, p65; NFAT1 and
652 NFAT2; RNA polymerase Ser2 phosphorylation, and Histone 3 lysine 9 trimethylation), as
653 well as Tat in the chromatin preparations of the active and latent cells. The ChIP assays were
654 performed by amplifying a 240 bp fragment spanning the enhancer-core promoter region in
655 the LTR using a semi-quantitative PCR and also using an independent Taqman probe-based
656 real-time PCR amplifying a 127 bp region spanning the NF-κB and Sp1 sites in the LTR
657 (Figure 10A).

658 The comparative analysis of the nature of the host factors recruited between the active and
659 latent promoters was highly reproducible and consistent between the 4- and 3-κB LTRs
660 (Figures 10C, 10D, 10F, and 10G). While the transcription promoting host factors, p65 and

NFAT2, and epigenetic marks RNA Pol II S2, were found associated with the active viral promoters at significantly higher levels, the transcription repressive factors, p50, NFAT1, and epigenetic marks H3K9Me3 were preferentially associated with the latent viral promoters. That the p50-p65 heterodimer is transcription-promoting, the presence of a significantly higher concentration of p65 at the active promoter is expected (33-35). On the other hand, the preferential association of p50 with the latent promoter is suggestive of the formation of the p50 homodimer, a known transcription suppressor (36). Similarly, our data are also in agreement with the previous reports regarding the transcription suppressive and supportive functions of NFAT1 and NFAT2, respectively (37-39).

The most crucial finding of the present study is the detection of the association of the Tat protein with the latent LTR. The Tat protein was found associated with the latent 4-κB and 3-κB promoters at levels 1.7- and 3-folds lower, respectively, as compared to their active counterparts. The results were reproducible and consistent in the semi-quantitative PCR-based ChIP analyses between the two strong viral promoters (Figures 10C and 10F). The data were also consistent between the conventional and the quantitative real-time PCRs performed following immunoprecipitation (Figures 10D and 10G). To the best of our knowledge, the present study is the first one to demonstrate the association of Tat with the latent LTR. The above ChIP data were generated using a commercial rabbit polyclonal anti-Tat antibody (Cat # ab43014, Abcam). The data were also reproducible when two additional mouse monoclonal anti-Tat antibodies targeting different epitopes in Tat (Cat # 7377 and # 4374, NIH AIDS reagent program, Maryland, USA) were used in the assay (Figure 10H). All the three different anti-Tat antibodies furnished positive ChIP signals for Tat at both the latent viral promoters (3- and 4-κB), over and above the respective IgG-isotype controls.

685 **Discussion**

686 **The significance of Tat recruitment to the latent LTR:**

687 The primary finding of the present work is the identification of a positive correlation between
688 the transcriptional strength of the LTR and faster latency kinetics via the mediation of
689 proportionately enhanced Tat concentration. We found that at the time of commitment
690 towards latency and at subsequent time points, the intracellular concentration of Tat is not a
691 limiting factor, thus, ruling out the possibility that the limiting levels of Tat underlie latency
692 establishment. To exert a positive or negative influence on the LTR, Tat must be present in
693 the nucleus and recruited to the viral promoter. Using three different experimental strategies,
694 the flow analysis of the Tat-RFP fusion protein (Figure 7), indirect immunofluorescence
695 (Figure 8, and a proximity ligation assay (Figure 9C), we successfully demonstrated the
696 presence of Tat in the nucleus of the latent cell, through the successive stages of latency
697 establishment. The presence of Tat could be detected in both the nuclear and cytoplasmic
698 compartments by confocal microscopy. Additionally, using ChIP, we could ascertain the
699 recruitment of Tat to the latent LTR using three different anti-Tat antibodies, although Tat
700 levels in the latent nuclei were typically inferior to those of the active nuclei (Figure 10).
701 Furthermore, a weak but discernible signal of the Tat-transcripts was evident in the latent
702 fractions of the bimodal clones of both the strong LTRs used in the assay (Figures 5F and 5J).
703 All these data are strongly suggestive that Tat plays a direct role in promoting latency.
704 Unfortunately, our attempts at adopting PLA to suspension cells were not successful. How
705 Tat is recruited to the chromatin complex needs to be determined. A few studies previously
706 showed the direct binding of Tat to extrachromosomal HIV-1 promoter and proviral DNA
707 (40, 41); however, the tethering of Tat to the nascent TAR element, as a part of the paused
708 RNA PolII complex proximal to the latent promoter (42), is a more likely possibility.
709

The underlying mechanisms regulating HIV-1 latency remain enigmatic:

There have been several attempts to understand HIV-1 latency as this question contains direct relevance for clinical management and viral purging (43). The complexity of HIV-1 latency has led to two distinct schools of thought to explain the phenomenon - the hypothesis of 'epiphenomenon' where the host environmental factors including the epigenetic modifications play the deterministic role (1, 44), and that of 'viral circuitry' where decision making is hardwired in the intrinsic Tat-LTR regulatory circuit (7, 9). The two models, which need not necessarily be mutually exclusive, have been supported by considerable experimental evidence but also have specific limitations.

Experimental evidence for epigenetic modifications controlling HIV-1 latency is available from studies using clonal cell populations typically harboring sub-genomic viral reporter vectors (45). The major limitation of this experimental model is the prolonged periods required for the cells to establish latency. The majority of individual clonal populations reach 50% of latency on an average in 30 to 80 days, which probably is not representative of the kinetics of natural latency. Given the cytotoxic properties of the viral products and the immune response, and a relatively short life-span of infected T cells (~ 2.2 days) (46), viral gene expression is expected to drive viral evolution towards rapid, not prolonged, latency establishment, in natural infection. Additionally, it is also not understood how epigenetic silencing of an active viral promoter is ever achieved, especially in the presence of abundant quantities of Tat.

The contrasting model explaining HIV-1 latency based on the intrinsic and virus-driven stochastic phenomenon is also supported by compelling experimental evidence (7, 9). The 'feedback-resistor' module (12), considers a single type of chemical modification,

735 acetylation, and deacetylation, of Tat, serving as the 'resistor' or dissipater of the positive
736 transcription loop to ensure a stable latent state. The model doesn't take into account several
737 other PTMs of Tat. Whereas di-methylation of the lysine residues at positions 50 and 51 (47)
738 and the arginine residues at positions 52 and 53 (48) can suppress Tat-transactivation, mono-
739 methylation of the lysine residues shows the opposite effect (49). Importantly, methylated Tat
740 is expected to have enhanced cellular stability with implications for latency (50). In addition
741 to acetylation, the phosphorylation of multiple serine and threonine residues can
742 cooperatively enhance Tat transactivation (51, 52). Polyubiquitination of Tat can also
743 enhance the stability of Tat, thereby augmenting its transactivation function (53). Apart from
744 the chemical modifications, Tat is also known to be inactivated by the propensity of the
745 protein to make dimer and multimer forms, although experimental evidence is scanty in this
746 regard (54). Furthermore, the differential forward and reverse reaction kinetics of Tat
747 acetylation have been evaluated only in HeLa cells, but not in cells of physiological relevance
748 to HIV-1 infection (55). Weinberger et al., also analyzed the feedback strength in terms of the
749 noise autocorrelation function and demonstrated that a stronger Tat feedback would yield
750 transcriptional pulses of longer durations leading to cell lysis while the weaker Tat feedback
751 and the Tat-independent transcription would generate shorter transcriptional pulses leading to
752 latency (8). The model, however, doesn't reconcile to the fact that a small proportion of T
753 cells can still escape cell death following Tat-mediated transcription and establish a viral
754 reservoir (56). In summary, despite significant experimental evidence, the question regarding
755 the critical deterministic factor(s) regulating HIV-1 latency remains unresolved.
756
757 **Subtype-associated molecular features may offer vital clues to HIV-1 latency:**
758 Although the fundamental constitution of the HIV-1 promoter is highly conserved among the
759 various genetic subtypes of HIV-1, there exist many subtype-specific molecular features that

760 may modulate gene expression considerably. Such differences are evident in the copy-
761 number and nucleotide sequences of different TFBS especially those of USF, c-Myb, LEF-1,
762 Ets1, NF-AT, Ap-1, NF-κB, and Sp1 binding sites, and regulatory elements such as the
763 TATA box and the TAR element (57-59). These regulatory elements play critical roles in
764 positively regulating the basal and inducible levels of viral transcription (60, 61). Most of the
765 TFBS, especially the AP-1, USF, NFAT, NF-κB, and Sp-1 motifs also play a critical role in
766 regulating viral latency by recruiting chromatin-modifying complexes and transcription
767 suppressing factors such as the histone deacetylases (HDACs) to the viral promoter (62-66).
768
769 Of the various TFBS, both NF-κB and Sp-1 motifs are represented by multiple and tandem
770 binding sites in the LTR, and, play crucial roles in regulating gene expression and latency
771 (36, 67-69). The most striking feature in the HIV-1C LTR is the copy-number difference of
772 NF-κB motifs, the sequence variation of the additional κB motifs (25), and the associated
773 sequence variation of the Sp1III site (32). We demonstrated previously that NF-κB site
774 duplication is unique for HIV-1C not recapitulated by any other HIV-1 genetic family.
775 Importantly, in HIV-1C, a unique NF-κB motif (the C-κB element, GGGGCGTTCC) and a
776 genetically distinct and subtype-specific Sp1III site are located at the core of the promoter,
777 and the two elements establish a functional association in enhancing HIV-1C transcription
778 (32).
779
780 HIV-1C could serve as an ideal model to ask whether transcriptional strength can affect viral
781 latency, a property not explored previously probably due to the absence of NF-κB copy-
782 number variation in non-HIV-1C subtypes. The rapid expansion of the 4-κB viral strains in
783 India in a short period of ten years, from 2% to 25 – 35%, is quite surprising (25). The ATF
784 model we used here also demonstrated a perfect positive correlation between the number of

NF-κB binding sites in the LTR and the viral transcriptional output in the form of EGFP and Tat transcripts (Figure 2) suggesting that all the four NF-κB binding sites in the LTR are functional. In this backdrop, it remains intriguing why HIV-1C strains require enhanced transcriptional strength, and despite having a strong promoter, how do these viral strains establish and maintain latency while the other HIV-1 genetic subtypes do not adopt such an evolutionary strategy.

Reciprocal binding of host-factors at the active and latent promoters:

Gene expression is the outcome of multiple layers of regulatory events consisting of the *cis*-acting TFBS and the *trans*-acting chromatin remodelers, viral factors, especially Tat, epigenetic marks, and a cross-talk between a wide array of proteins, ultimately leading to diverse phenotypic outcomes. Numerous studies attempted to examine how the nature of the host factor complexes recruited at the LTR regulates the dynamic switching between the active and latent states (45, 70). In an elegant analysis, Burnett et al., used PheB cells derived from the GFP^{Mid} parental Jurkat cells (analogous to GFP^{Dim} in (7) and GFP^{Low} in the present study) and compared the nature of cellular complexes recruited between transcriptionally active and latent cells (26). This study demonstrated a non-overlapping function of the two genetically identical NF-κB sites in regulating transcriptional activation versus suppression. We employed a similar experimental strategy with the exception that we used the $EGFP^{High}$ clonal cell populations (the bimodallers, Figure 5B) that manifested a bimodal phenotype of EGFP expression. The $EGFP^{High}$ and the $EGFP^{-}$subsets of bimodal cell clones offered a significant technical advantage of normalizing the inherent differences in cellular parameters.

The preferential binding of p50 and p65 (RelA) at the latent and active promoters ascertained the repressive and inducing functions of p50-p50 homodimer and p50-RelA heterodimer

respectively, of HIV-1 transcription (Figure 10) (26, 35, 36). Unlike the NF-κB proteins, the impact of individual NFAT members on HIV-1 latency has not been examined in great detail. To the best of the knowledge, the present study is the first to demonstrate a reciprocal binding pattern of NFAT1 and NFAT2 at the active and latent promoters, respectively, in the context of clonal cells. Since NF-κB and NFAT factors share overlapping sites (71-73), NFAT may have a significant influence on latency in HIV-1C. Furthermore, the NF-κB sites in the C-LTR (F, H, and C-κB sites) are genetically different, adding to the multitude of possible combinations. Targeted inactivation of each κB site, one at a time, followed by ChIP, may provide meaningful insights into the contribution of each κB sequence to diverse signaling pathways and HIV-1C latency.

The key finding of the present study, however, is the detection of the association of the Tat protein with the latent LTR. The results were highly reproducible and consistent between the two strong viral promoters (Figure 10). The data were also consistent between the conventional PCR and the quantitative real-time PCR performed following immunoprecipitation. The data were reproducible when three different anti-Tat antibodies targeting different epitopes in Tat were used in the assay. The Tat protein was found associated with the active 4-κB and 3-κB promoters at 1.7- and 3-folds higher, respectively, as compared to their latent counterparts. To the best of our knowledge, the present study is the first one to demonstrate the association of Tat with the latent LTR, albeit at a lower intensity as compared to the active promoter.

The negative feedback circuits represent a powerful and common strategy biological systems exploit to regulate gene expression:

834 Negative feedback circuits can rapidly switch off signaling cascades; therefore, this mode of
835 gene regulation represents the most common strategy biological systems exploit to regulate
836 gene expression (74). Molecules of biological significance controlling powerful signaling
837 cascades such as cytokines and transcription factors, often attenuate their own production
838 using negative feedback loops. The transcription factor NF-κB that controls the expression of
839 numerous cellular factors that regulate a wide variety of cellular processes, down-regulates
840 self-expression by activating the inhibitor protein IκBα (75). Likewise, interleukin-2 (IL-2),
841 the most potent cytokine that regulates T cell viability and proliferation, limits self-
842 production by activating the expression of a FOXP3-mediated negative feedback loop (76).
843 Given that the latency establishment is central for HIV-1 survival towards evading immune
844 surveillance and minimizing cytotoxicity, an active molecular mechanism would be
845 necessary to suppress gene expression from the LTR rapidly. The decision making to achieve
846 such a critical phase of the viral life cycle must be an intrinsic characteristic of the MTRC of
847 the virus; it couldn't be left to stochastic phenomena or epiphenomena regulated by cellular
848 events. That the MTRC of HIV-1 comprises of only two elements – the LTR and Tat, and
849 that the latter is the only factor encoded by the virus, Tat is the viral factor best positioned to
850 regulate viral transcription and transcriptional silence both, perhaps at different phases of the
851 viral life cycle following integration. Data presented here using two different latency cell
852 models are not only consistent with this critical biological function ascribed to Tat but also
853 provide additional information on latency. In the present work, we examined the latency
854 profile only in the context of HIV-1C, and its validity must be examined in other genetic
855 families of HIV-1.
856
857 Based on several facts, the master regulator of the virus is well-positioned to be a potential
858 candidate to impose negative feedback on the LTR, in a temporal fashion; including the

absence of a known transcription suppressor encoded by the virus, the ability of Tat to constitute the master regulatory circuit of the virus in combination with the LTR in the absence of other viral factors, the presence of Tat in the latent cell detected reproducibly and also recruited to the latent promoter, and the identification of a positive correlation between the transcriptional strength of the LTR and the rate of latency establishment.

A Tat-dependent negative feedback mechanism to establish latency?

Based on the present study, we propose a novel model for the transcriptional repression of HIV-1 through a Tat-negative feedback mechanism. The attenuation of Tat-positive feedback signaling has been proposed to cause the LTR silencing, triggered by extracellular cues (deterministic model) or limiting Tat levels probabilistically (stochastic model) (7, 8, 12, 26). In either case, Tat concentration gradually falls below a threshold insufficient for self-renewal or successful transcriptional elongation.

Our data allude to a concentration-dependent inter-conversion of the active form of Tat to a repressive form, the latter competing with the former, strengthening a negative-feedback circuit leading to the rapid silencing of the promoter (Figure 11). We propose that the autonomous Tat-feedback loop initially favors the steady accumulation of Tat molecules to enhance transcription. Subsequently, at a point when Tat intracellular concentration surpasses a specific threshold level, Tat switches to the suppression mode down-regulating transcription, possibly depending on differential PTM modifications of Tat itself. Hence, our model proposes that the strong promoters (3- and 4-κB LTRs) characterized by a stronger Tat-feedback, can initiate a rapid transcriptional silence as compared to the weak promoters (2-, 1- and 0-κB LTRs).

884 Our data raises several important questions related to HIV-1C latency, which were beyond
885 the scope of the present study. Is the LTR of HIV-1C likely to continue to acquire additional
886 copies of NF-κB and/or other transcription factor binding sites to augment transcriptional
887 strength further? Of note, unpublished data from our laboratory (Bhange D et al, unpublished
888 data) demonstrate a recent trend of emergence of at least 10 different types of TFBS variant
889 HIV strains in India. Further, how the variant NF-κB motifs unique for HIV-1C modulate
890 viral latency? Answers to these questions will shed light on the mechanism of HIV-1 latency
891 and likely to help design novel therapeutic strategies to purge HIV infection.
892
893 We acknowledge a few technical limitations of the present work that were beyond our
894 control. Our attempts to extend the observations to full-length HIV-1C molecular clones were
895 not successful for two main reasons- (1) the lack of good molecular clones representing HIV-
896 1C (only four molecular clones of HIV-1C are available). (2) Additionally, unlike NL4-3, an
897 HIV-1B molecular clone mostly used in the field, the few available HIV-1C clones do not
898 lend themselves for significant molecular manipulation of any kind; the in vitro infection
899 property of the HIV-1C viral strains is significantly low compared to other subtypes (please
900 see a recent review (77), which highlights this problem of HIV-1C explicitly), Further, the
901 engineering of a fluorescent protein as a reporter will make these clones nearly unviable. Our
902 data were derived from Jurkat cell infection- the most popular cell model in the field (26, 45,
903 78-81). Latently infected primary cells in vivo are extremely rare in the order of 10^{-6} (1), and
904 it would be a daunting task to isolate Tat from such a small population. Further, to examine
905 latency establishment in primary cells, a stable cell pool must be generated, reactivated. Such
906 manipulations in primary cells would require at least 6 to 8 weeks, a time frame not
907 conducive to sustaining primary cells in culture. Primary cell models have traditionally been
908 used to examine latency reversal and to evaluate latency-reversing agents but rarely to study

latency establishment. A suitable, long-lasting primary cell-based model to study the mechanisms involving HIV-1 latency establishment is an absolute requirement, and we have been optimizing this model in our laboratory for future studies. Additionally, we have been raising antibodies specific to defined PTM of Tat to investigate how Tat-PTM may modulate HIV-1 latency.

Materials and Methods

Cell culture

Jurkat cells were maintained in RPMI 1640 medium (R4130, Sigma-Aldrich, St. Louis, USA) supplemented with 10% fetal bovine serum (RM10435, HiMedia Laboratories, Mumbai, India), 2 mM glutamine (G8540, Sigma-Aldrich), 100 units/ml penicillin G (P3032, Sigma-Aldrich) and 100 g/ml streptomycin (S9137, Sigma-Aldrich).

The human embryonic kidney cell lines HEK293 and HEK293T were cultured in Dulbecco's modified Eagle's medium (D1152, Sigma-Aldrich) supplemented with 10% FBS. All the cells were incubated at 37^0C in the presence of 5% CO_2.

Design and construction of HIV-1C reporter vector panels

Autonomous Tat-feedback (ATF) model: The pLGIT reporter vector (HIV-1 LTR-EGFP-IRES-Tat; (7)) was a kind gift from Dr. David Schaffer (University of California, USA), in which the two different elements, the 3'LTR, and Tat, were of HIV-1B origin (NL4-3). We substituted these two elements with analogous counterparts of HIV-1C origin (Indie_C1-Genbank accession number AB023804) and referred to the vector as pcLGIT (cLTR-EGFP-IRES-cTat; (32)). Using the pcLGIT backbone, we constructed a panel of five reporter vectors containing varying copies of functional NF-κB motifs, ranging from 0 to 4 (the p911a

vector series). First, an LTR containing four tandem NF-κB motifs (FHHC-LTR; H-GGGACTTTCC, C- GGGGCGTTCC, F- GGGACTTTCT; variations among the κB-motifs underlined), was generated in an overlap-PCR using the LTR of Indie_C1 as the template. The additional 22 bp sequence constituting the F-κB motif was adopted from the HIV-1C molecular clone BL42-02 (GenBank accession No. HQ202921). The amplified FHHC-LTR was inserted into pcLGIT vector, substituting the original 3'-LTR. Subsequently, using the overlap-PCR, inactivating point mutations were introduced sequentially into the 'FHHC' (4-κB) LTR, to generate the other members of the panel: OHHC (3-κB), OOHC (2-κB), OOOC (1- κB) and OOOO (0-κB) (Figure 2A). Of note, the inactivation mutations only introduced base substitutions, not deletions, keeping the length of the viral promoter constant among the variant viral vectors. The mutated κB-motif 'O' contains the sequence TCTACTTTTT (underlined bases represent inactivating mutations). The variant LTR fragments were cloned directionally between the XhoI and PmeI sites present on the outer primers- N1990 FP (5'-GCGTACCTCGAGTGGAAGGGTTAATTTACTCCAAGAAAAGGC-3') and N1991 RP (5'-TATGTCGTTTAAACCTGCTAGAGATTTTCCACACTACCAAAAGGGTCTGAG-3') thus, substituting the original 3'-LTR of pcLGIT. Therefore, the members of the vector panel are genetically identical except for the differences in the functional NF-κB motifs in the LTR. The internal primer sequences to generate the point mutations in the LTR variants are mentioned in Table 1. The 3' LTR sequences of all the panel members were sequence-confirmed, and the expression of EGFP was ascertained in HEK293T cells.

A second panel of the five variant viral vectors, analogous to the p911a panel was also constructed using the pcLdGIT backbone, where EGFP was substituted with d2EGFP, a variant form of the fluorescent protein characterized by the shorter half-life (p911b vector

series). First, the d2EGFP ORF was amplified from the pCAG-GFPd2 plasmid (#14760, Addgene, Massachusetts, USA) using the primer pair- N1142 FP (5'-CAGGAATTCGATGCTACCGGTCGCCACCATG-3') and N1143 RP (5'-TCCTACTAGTAGGATCTGAGTCCGGACTACACATTGATCC-3') and directionally cloned between the AgeI and BspE1 sites to replace the EGFP with the d2EGFP reporter gene in the pcLGIT backbone. To generate the p911b panel, the variant LTRs of the p911a panel were transferred directionally to the pcLdGIT vector backbone between the PmeI and XhoI sites, thus substituting the original 3'-LTR. The expression of d2EGFP from all the vectors of the p911b panel was verified using HEK293T cells.

Tunable Tat-feedback (TTF) model: In the TTF model, HIV-1C LTR regulates the co-expression of d2EGFP and Tat-RFP fusion protein from the vector pcLdGITRD (cLTR-d2EGFP-IRES-cTat:RFP:DD). The 5' LTR in the pcLdGITRD vector transcribes a single transcript encoding d2EGFP and a 1,314 bp long fusion cassette separated by an IRES element. The fusion cassette is a combination of three different ORFs- (i) the cTat expression segment (BL4-3, GenBank accession number FJ765005.1), (ii) the ORF of DsRed2-RFP, and (iii) the FKBP destabilization domain (DD) (28). The three components of the 'Tat:RFP:DD' cassette were independently amplified using appropriate templates and primers, and, finally, using an overlap PCR, the fusion ORF was generated (primer sequences provided in Table 1). The Tat ORF from the pcLdGIT-3-κB vector (p911b series; ATF model) was replaced with the 'Tat:RFP:DD' ORF, thus, generating the pcLdGITRD-3-κB viral vector. pcLdGITRD-3-κB was subsequently used as the parental vector to construct the other member-pcLdGITRD-1-κB of the panel p913 (Figure 6A) by cloning the respective 3'LTRs between

PmeI and XhoI in the pcLdGITRD backbone. The d2EGFP expression from the two members of the panel p913 was confirmed in HEK293T cells.

Shield1 dose-dependent Tat:RFP:DD expression from the pcLdGITRD vector (TTF model) in HEK293T cells

The FKBP DD-tag in the pcLdGITRD construct marks the 'Tat:RFP:DD' fusion protein for rapid degradation through the proteasome pathway (28). However, 'Shield1', a 750 kD cell-permeable ligand can bind the DD motif and rescue the fusion cassette from rapid processing in a dose-responsive manner with minimum off-target effects (29). Thus, by changing the concentration of Shield1 in the culture medium, the pcLdGITRD construct permits fine-tuning of the intracellular concentration of Tat without altering the transcriptional strength of the LTR. To validate the Shield1 dose-dependent Tat:RFP:DD expression, approximately 0.6 million HEK239T cells were transfected with 1 μg pcLdGITRD-3-κB vector in each well of a 12-well culture dish and treated with varying concentrations (0, 0.5, 1.0, 2.5, 4.0 and to 5.0 μM) of Shield1 (#632189, Takara Clontech). After 48 h of transfection, the expressions of both DsRed2-RFP and d2EGFP were recorded using a fluorescent microscope.

Generation of pseudotyped reporter virus and the estimation of relative infectious units (RIU)

Pseudotyped reporter viruses were generated in HEK293T cells. Each viral vector was transfected together with the 3rd generation lentiviral packaging vectors using the standard calcium phosphate protocol (82). Briefly, a plasmid DNA cocktail consisting of 10 μg of individual viral vector (NF-κB motif variants), 5 μg psPAX2 (#11348; NIH AIDS reagent

program, Maryland, USA), 3.5 µg pHEF-VSVG (#4693; NIH AIDS Reagent program) and 1.5 µg pCMV-rev (#1443; NIH AIDS Reagent program) was transfected in a 100 mm dish seeded with HEK293T at 30% cell confluence. pCMV-RFP (0.2 µg) was used as an internal control for transfection. Six hours post-transfection, the medium was replenished with complete DMEM. Culture supernatants were harvested at 48 h post-transfection, filtered using 0.22 µ filter and stored in 1 ml aliquots in a deep freezer for future use.

The RIU of the pseudotyped reporter viruses was quantified in Jurkat T-cells by measuring EGFP or d2EGFP expression by flow cytometry. Precisely, 3 x 10^4 Jurkat cells in each well of a 12-well tissue culture plate were infected with individual viral stocks serially diluted 2-fold (from 10 xd to 80 xd) in a total volume of 1 ml of 10% RPMI containing 25 µg/ml of DEAE-Dextran. Six hours post-infection, the cells were washed and replenished with 1 ml of complete RPMI. Post 48 h, the cells were activated with a combination of 40 ng/ml PMA (P8139, Sigma Aldrich), 40 ng/ml TNFα (T0157, Sigma-Aldrich), 200 nM TSA (T8552, Sigma Aldrich) and 2.5 mM HMBA (224235, Sigma-Aldrich) for 18 h, following which the percent $EGFP^+$ or $d2EGFP^+$ cells were analyzed using a flow cytometer (BD FACSAria III sorter, BD biosciences, New Jersey, USA). Following this, titration curves were constructed and analyzed for 5-10% infectivity of the cells by regression analysis, which would correspond to ~0.05-0.1 RIU. For the TTF model, cells were maintained in 1µM Shield1 throughout the procedure.

Viral gene-expression analysis

Viral gene-expression levels were compared among the LTR variant strains of the pcLGIT panel (ATF model). Towards this, approximately one million Jurkat cells were infected with each viral strain of the panel independently at an RIU of ~0.5–0.6. Three days following

infection, the cells were activated using a cocktail of global T-cell activators (40 ng/ml PMA + 40 ng/ml TNFα + 200 nM TSA + 2.5 mM HMBA) and 24 hours following activation, EGFP fluorescence (mean fluorescence intensity or MFI) was estimated for both the uninduced and activated cells using flow cytometry. Tat transcript levels of the control and activated cells, were determined using a Tat RT-PCR (see below). Fold enhancements in EGFP, and Tat expression levels were obtained from the ratios of the EGFP-MFI values of the activated and control samples and similarly their relative Tat-mRNA values, respectively.

To compare the gene-expression levels from the LTR at different transcriptional strengths of Tat-feedback, modulated by the Shield1 concentrations (TTF model), approximately 0.3 million Jurkat cells in a 35 mm culture dish were infected with the cLdGITRD-3-κB viral strain at a p24 equivalent of 20 ng/ml. Twenty-four hours post-infection, the infected cells were washed and replenished with complete RPMI. The cells were then equally distributed into four wells of a 6-well plate and each well treated with either 0, 0.5, 2.5, or 5.0 μM Shield1. After 48 hours, half of the cells from each Shield1 treatment were activated using the global T-cell activators, and 24 hours later, both the uninduced and activated fractions from each dose of Shield1 were subjected to d2EGFP and Tat-transcript expression analysis using flow cytometry and RT-PCR, respectively.

FACS sorting and the generation of stable Jurkat cells and clonal lines

ATF model: Individual, NF-κB variant, pseudotyped viral stocks of the cLGIT/cLdGIT panel were added to 1 x 10^6 Jurkat cells in a 35 mm culture dish, at an RIU of ~0.05-0.1 in a total volume of 2 ml complete RPMI supplemented with 25 μg/ml DEAE-Dextran. After six hours of infection, cells were washed to remove DEAE-Dextran and transferred to 5 ml of complete RPMI medium in a T-25 flask and maintained under standard culture conditions.

The infected cell pools were expanded over seven days and induced with the global T-cell activation cocktail as mentioned above. After 18 h of activation, total $EGFP^{+}$ (MFI $>10^3$ RFU), $EGFP^{High}$ (MFI $>10^4$ RFU), or $d2EGFP^{High}$ (MFI ~0.5 X 10^3 – 0.5 X 10^4) cells were FACS sorted from respective cell pools depending on the subsequent viral latency assays. A small aliquot of the sorted cell population was re-analysed to confirm the purity of the sorted cells. Each sorted cell pool with a stable EGFP/d2EGFP expression represented a mixed population with random proviral integrations with the corresponding NF-κB variant strain.

Stable clonal cell lines of the cLGIT variant panel (expressing EGFP) were established by sorting a single cell per three wells in a 96-well plate. Each well of the collection plate contained 100 µl of a mix of equal proportions of complete- and the spent-RPMI media. The cells were diluted to a cell density of 0.1 x 10^6/ml before the sort.

TTF model: 1 x 10^6 Jurkat cells were infected with the sub-genomic cLdGITRD viral strains (3- and 1-κB variants) at an RIU of ~0.1-0.2 in 1 ml of complete RPMI medium supplemented with 25 µg/ml of DEAE-dextran and 1.0 µM Shield1. Six hours post-infection, the infected cells (J-cLdGITRD) were washed and replenished with 1 ml of complete RPMI supplemented with 1 µM Shield1. Next, 72 h following the infection, the cells were induced with the previously mentioned T-cell activation cocktail for 18 h, and following the activation, the stable, $d2EGFP^{+}$ J-cLdGITRD cells were sorted.

The analysis of proviral integration frequency

A Taqman qPCR was used to determine the mean number of proviral integrations per cell using the genomic DNA extracted from the stable, J-cLGIT cell pools, and also from the

EGFP^{High} and EGFP^{-} subfractions corresponding to the representative bimodal clones of the 3-κB and the 4-κB variants. Genomic DNA was extracted from 1 x 10^6 stable cells using the GenElute mammalian genomic DNA kit (G1N350, Sigma-Aldrich) following the manufacturer's instructions. The extracted DNA was dissolved in TE, and the concentration was adjusted to 70 ng/µl. Five µl of this solution was equivalent to approximately 10^5 copies of the human genome. The stock DNA solution was subjected to a 10-fold serial dilution up to a final DNA concentration of 10^1 copies/5 µl and used as the template in the PCR. A 129 bp fragment spanning the R-U5 region of the HIV-1 5' LTR (+18 to +147) was amplified using the primer-probe combination N2208 FP, N2209 RP, and N2210 FAM (see Table 1 for the primer sequences) in a Taqman real-time PCR. A standard curve was established simultaneously using the genomic DNA extracted from the J-Lat 8.4 cells that contain a single proviral copy per cell (78). The proviral copy number of the query samples was then estimated using the regression analysis.

Generation of kinetic profiles of latency-establishment

ATF model: Kinetic curves of latency were established to compare the rates of promoter silencing among the NF-κB variant strains of the ATF panel. Towards this, the sorted cell pools (total EGFP^{+}, EGFP^{High,} or d2EGFP^{High}) were maintained under standard experimental conditions while a small aliquot was collected at regular intervals to monitor the EGFP/d2EGFP expression using the FACSAria III flow cytometer. Temporal kinetic profiles for % GFP^{+} cells and GFP-MFI were constructed and compared among the five NF-κB variants for the total EGFP^{+ve}, EGFP^{High} as well as the d2EGFP^{High} cells. The EGFP reporter gene having a longer half-life (~48 h) was measured every 4 days for 16-24 days while the

analysis of d2EGFP expression with a shorter half-life (~ 2h) was performed every 24 h following sorting, for 7 days.

Kinetic profiles of latency were established for the clonal lines of the cLGIT panel. The sorted, single $EGFP^{High}$ cells corresponding to each NF-κB variant strain were expanded to form clonal lines, and 16 such lines corresponding to each cLGIT viral variant were flow-analyzed for their EGFP expression profiles on Days 21 and 28 post sorting.

TTF model: Latency-establishment profiles at varied strengths of the Tat-feedback circuit were studied using the TTF model by altering the Shield1 concentrations in the culture medium. The sorted $d2EGFP^{High}$ cells corresponding to the cLdGITRD-3-κB (strong) and the cLdGITRD-1-κB (weak) LTR variants were divided into four separate fractions and maintained at four different concentrations of Shield1 (0, 0.5, 1 and 3 μM) under standard experimental conditions, while a small aliquot from all the fractions was collected every 24 h to monitor the expression of both d2EGFP and Tat-RFP using FACSAria III flow cytometer, for 7 days. Temporal kinetic profiles were constructed and compared among the two NF-κB variants as well as across the different concentrations of Shield1.

Live-dead analysis of cells

A live-dead, viability assay was performed to exclude the dead cells before every flow analysis. Cell samples were stained using the LIVE/DEAD™ fixable Red Dead Cell Stain Kit (#L34972, Molecular Probes, Thermo Fisher Scientific, Massachusetts, USA) following the manufacturer's protocol. Briefly, cell samples were harvested in a microcentrifuge tube, washed once with 1X PBS, and resuspended in 500 μl of 1:1,000 diluted live-dead stain. The

cells were then incubated for 30 mins at room temperature in the dark, following which they were washed, resuspended in 500 µl of RPMI supplemented with 2% RPMI and analyzed in the flow cytometer.

DNA cell-cycle analysis

Cell cycle analysis by quantitating DNA content was performed on the $EGFP^{High}$ and $EGFP^{-}$ subfractions of the bimodal clonal lines of the J-cLGIT-3- and 4-κB variants. The standard propidium iodide (PI) staining protocol was followed with slight modifications to minimize the quenching of the EGFP signal (83). Briefly, 1 X 10^6 cells were harvested in 1.5 ml microcentrifuge tubes and washed once with 1X PBS. The pellets were resuspended thoroughly in 1 ml fix solution (2% glucose and 2% paraformaldehyde in 1X PBS) and incubated on ice for 10 mins. The cells were then washed once with 1X PBS, resuspended in 100 µl of 1X PBS, and 900 µl of ice-cold 70% ethanol added dropwise with gentle vortexing. The fixed cells were incubated on ice for 1 h, washed with 1X wash solution (20 mM Hepes, 0.25% NP-40, 0.1% BSA in 1X PBS), supernatants aspired and resuspended in 500 µl of 1X PBS containing 10 µg/ml RNAse A and 20 µg/ml PI. This was followed by incubation in the dark for 30 mins at room temperature and analysis by flow cytometry. Pulse processing (pulse area vs pulse height) was used to exclude doublets, and debris and the gated singlets were applied on the PI histogram plot to determine the % cells in the G1, S, and G2/M phases.

Quality assurance and data analysis in flow cytometry

The BD FACSAria III sorter was optimized and calibrated before every operation (flow analysis or sorting) to ensure quality performance. The instrument was calibrated for optical laser alignment, fluorescence and light scatter resolution, and fluorescence detector sensitivity using the BD™ CS&T beads (#656504, BD Biosciences). Drop delay before every FACS sort was determined using the BD FACS™ Accudrop beads (#345249, BD Biosciences) while fluorescence linearity and doublet discrimination before DNA cell-cycle analysis were assessed using the BD™ DNA QC particles (#349523, BD Biosciences). Further, uniform PMT voltage parameters were set for every fluorescent channel using appropriate negative control samples to avoid variations in the MFI measurements at different time-points of the latency kinetics experiments.

All the flow cytometry data analyses were performed using FCS Express 4 and 6 versions (De Novo Software, Los Angeles, CA).

The analysis of the Tat-transcripts in stable Jurkat cells

We quantitated Tat transcript levels using a real-time PCR as a surrogate marker of the transcriptional status of the LTR during latency-establishment, or latency reversal. Total mRNA was extracted from 0.5 x 10^6 cells using a single-step RNA isolation reagent- TRI reagent (T9424, Sigma-Aldrich) at specified time points. Using random hexamer primers, 250-1,000 ng of extracted RNA was converted to cDNA in a reaction volume of 20 µl using the Tetro cDNA synthesis kit (BIO-65043, Bioline, London, UK). The cDNA was then amplified using an SYBR green RT-PCR kit (06924204001, Roche Products, Mumbai, India) for a 139 bp region in the Tat exon-1 using the primers- N1783 (5'-GGAATCATCCAGGAAGTCAGCCCGAAAC-3') and N1784 (5'-CTTCGTCGCTGTCTCCGCTTCTTCCTG-3'). The GAPDH RT-PCR was employed as an

internal control (primer pair N2232: 5'-GAGCTGAACGGGAAGCTCACTG-3' and N2233: 5'- GCTTCACCACCTTCTTGATGTCA-3'). The relative gene expression was calculated using the ΔΔCt method.

Indirect immunofluorescence of Tat

Immunofluorescence staining of Tat was performed at multiple time points during the establishment of viral latency in stable J-cLdGIT-3-κB cells characterized by strong d2EGFP fluorescence (MFI range 5 x 10^3 to 50 x 10^3). The sorted d2EGFP^{High} cells were considered as the D0 sample, and Tat-IF was performed subsequently at an interval of every 4 days. Approximately 3 x 10^6 cells were collected in a 1.5 ml vial, washed once with 1X PBS, and fixed with 2% paraformaldehyde in PBS for 10 min at room temperature with mild rocking. Fixed cells were re-washed with 1X PBS followed by permeabilization with 0.2% Triton-X-100 in PBS for 10 min with gentle and intermittent vortexing. Fixed and permeabilized cells were then washed again with 1X PBS and blocked with 4% BSA in PBS for 30 min at room temperature with mild rocking. The blocked cells were incubated with a rabbit, polyclonal anti-Tat antibody (ab43014, Abcam, Cambridge, UK) at 1: 250 dilution for 1h at room temperature followed by two PBS washes. This was followed by the incubation with 1: 500 dilution of Goat anti-rabbit Alexa Fluor 568 (A-11010, Molecular Probes) for 20 min in the dark at room temperature followed by a PBS wash. The nucleus was stained with 4 μg/ml of DAPI for 20 min in the dark at room temperature. Cells were washed twice and mounted on coverslips with 70% glycerol for confocal imaging. Images were acquired with a Zeiss LSM 880 confocal laser scanning microscope with Airyscan using a Plan Apochromat X63/1.4- oil immersion objective and analyzed using the ZEN 2.1 software. For imaging single cells, a 4X higher zoom was applied. The fluorescent cut-off for d2EGFP expression was determined

using uninfected Jurkat control, while that for Tat-Alexa 568 expression was set using the infected but no-primary Tat antibody control. At each time-point, 150 cells were analyzed; fluorescent intensities (AU) for d2EGFP and Tat-Alexa 568 expressions independently determined for the nuclear and extra-nuclear compartments of the cells and temporal curves generated.

The proximity ligation assay

We used an in situ proximity ligation assay (PLA) to detect Tat in HEK293 cells independently infected with the cLdGIT-3- and 4-κB reporter virus. The assay was performed using a commercial kit (Duolink In Situ Red Starter kit Mouse/Rabbit, #DUO92101, Sigma-Aldrich) following the instructions of the manufacturer. Briefly, a heterogeneous population of HEK293 cells harboring both active and latent virus (cLdGIT-3-κB or 4-κB), marked by the presence or absence of green fluorescence, respectively, were seeded on glass coverslips and allowed to grow to 60-70% confluence. The evenly distributed cells on the coverslip were fixed with 4% paraformaldehyde for 20 min at room temperature, permeabilized with 0.1% Triton-X-100 for 10 min at room temperature and washed thrice with 1X PBS. This was followed by blocking for one hour using the reagent supplied in the kit. The blocked cells were then treated with the rabbit polyclonal anti-Tat antibody at 1: 250 dilution (Catalog no. ab43014, Abcam) in combination with the mouse monoclonal anti-Tat antibody at 1: 250 dilution (Catalog no. 7377, NIH AIDS reagent program, Maryland, USA). The cells were incubated with a pair of probes (the PLA probe Anti-Mouse MINUS; DUO92004 and PLA probe Anti-Rabbit PLUS; DUO92002) in a 40 µl reaction volume, for one hour at 37^0C followed by washing twice with 500 µl of wash buffer A for 5 min each time. The ligation and amplification reactions were performed as per manufacturer's

instructions using the Duolink In Situ Detection reagents Red (Catalog no. DUO92008). The DAPI-supplemented mounting medium (Catalog no. DUO82040, supplied in the PLA kit) was used for mounting the cells. No-primary and single antibody controls were used to assess non-specific PLA spots. Imaging of the cells was performed using a Zeiss LSM 880 confocal laser scanning microscope with Airyscan fitted with a Plan Apochromat 63X/1.4 oil immersion objective. Signal intensities of the PLA positive spots were quantitated manually using the Image J software. A total of 164 cells were analyzed from the d2EGFP^{+} category (128 from the 4-κB and 36 from the 3-κB sample) while 168 cells were analyzed from the d2EGFP^{-} category (123 from the 4-κB and 45 from the 3-κB sample) to compare the number of PLA dots per cell between the two phenotypes.

The primary antibody pair, the rabbit polyclonal anti-Tat (ab43014, Abcam) and mouse monoclonal anti-Tat (7377, AIDS reagents program) antibodies, was validated for Tat specificity before performing PLA in stable HEK293 cells harboring the cLdGIT-3- and 4-κB proviruses. Approximately 0.5 x 10^6 HEK293T cells in each well of an 8- micro chambered glass slide (80826, ibidi, Grafelfing, Germany) were transfected with either 800 ng of pcLGIT vector (B-Tat) or 200, 400 or 800 ng of pcLGIT vector (C-Tat). After 48 hours of transfection, Tat-PLA was performed as detailed above. Confocal images were captured using the same model of a confocal microscope and identical parameters, as mentioned above. Image J software was used to measure d2EGFP intensity (AU) and manual quantitation of Tat-PLA spots from 25 cells corresponding to each dose of pcLGIT vector.

Chromatin immunoprecipitation assay

We used a chromatin preparation equivalent of 2 x 10^6 cells (either EGFP^{High} or EGFP^{-ve}) for each immunoprecipitation assay, as described previously (32). Briefly, 2 x 10^6 Jurkat cells

collected in a 1.5 ml vial were washed with 1X PBS, resuspended in 1 ml of RPMI supplemented with 1% formaldehyde and incubated with gentle agitation for 10 min at room temperature. The cross-linking reaction was quenched by incubating the cells with 0.125 M glycine for 5 min with mild agitation at room temperature followed by centrifugation at 3,000 rpm for 5 min at 4^0C with a subsequent PBS wash (containing 0.01X protease inhibitor cocktail or PIC; #11836170001, Roche Applied Science, *Indianapolis*, USA). Following the complete removal of PBS, the cells were resuspended in 100 µl of ice-chilled lysis buffer (1% SDS, 50 mM Tris buffer, pH 8.0, 10 mM EDTA) and incubated on ice for 20 min with occasional mixing of the lysate using a wide-bore tip. The lysate in each vial was subjected to 22 cycles of sonication at the high mode, using 30-second-ON followed by a 30-second-OFF pulse scheme in the Bioruptor plus sonicator (UCD-300, Diagenode, Liege, Belgium) containing pre-chilled water. The sonicated lysate was centrifuged at 12,000 rpm for 10 min at 4^0C to remove any cellular debris; the clear supernatant was transferred to a fresh 1.5 ml vial and stored at -80^0C until use. One-tenth of the lysate (10 µl) was used to confirm the shearing of chromatin to generate 200-500 bp fragment sizes. Each IP comprised of 100 µl of lysate and 2 µg of an antigen-specific antibody against p50 (ab7971, Abcam, Cambridge, UK), p65 (ab7970, Abcam), NFAT1 (ab2722, Abcam), NFAT2 (ab2796, Abcam), HIV-1 Tat (ab43014, Abcam or #7377, NIH AIDS reagent program or #4374, NIH AIDS reagent program), RNA Pol II CTD phospho S2 (ab5095, Abcam), or H3K9 Tri Meth (ab8898, Abcam). The ChIPed DNA was amplified using the primer pair N1054 FP (5'-GATCTGAGCC(T/C)GGGAGCTCTCTG-3') and N1056 RP (5'-TCTGAGGGATCTCTAGTTACCAGAGTC-3') spanning a 240 bp sequence within the enhancer-core promoter region in the LTR. The amplified DNA fragments were subjected to agarose gel electrophoresis, and the band intensities were normalized using the percent-input method to compare differential recruitment of each transcription factor at the active vs. latent

promoter. To enhance the sensitivity of the assay, TaqMan qPCR was performed using the ChIP-DNA and the primer-probe combination- N2493 FP, N2215 RP, and N2492 Hex (refer to Table 1). The final data were evaluated using the percent input method.

Statistics

Statistical analyses were performed using GraphPad Prism 5.0 software. The statistical tests used to calculate *P* values are indicated in the corresponding figure legends.

Acknowledgements

We thank Prof. Tapas Kumar Kundu (JNCASR, India) and Dr. Ravi Manjithaya (JNCASR, India) for intellectual discussions. We thank Dr. Uttara Chakraborty, S.L. Swaroopa Yalla and Dr. Narendra Nala of the flow cell at JNCASR, Suma B.S of the Confocal Imaging Facility and Anitha G. of the Sequencing Facility at JNCASR, India. We thank Neelakshi Varma and Surabhi Jirapure for initial help in establishing the latency models. Several reagents were obtained through the AIDS Research and Reference Reagent Program. This work was supported by grants to U.R. from the Department of Biotechnology (DBT), Government of India (DBT grant no. BT/PR7359/29/651/2012); National Institute of Health (NIH), USA (Grant No. NIDA 5RO1DA041751-02), and intramural funds from JNCASR.

Author contributions

S.C., conception and design, acquisition of data, analysis and interpretation of data, drafting or revising the article, and providing essential unpublished data; **M.K.**, acquisition of data, analysis and interpretation of data, and providing essential unpublished data; **U.R.**, conception and design, fund acquisition, validation, writing, reviewing and editing the article.

Competing Interests

We declare that no competing interests exist.

References

1. Chun T-W, Carruth L, Finzi D, Shen X, DiGiuseppe JA, Taylor H, Hermankova M, Chadwick K, Margolick J, Quinn TC. 1997. Quantification of latent tissue reservoirs and total body viral load in HIV-1 infection. Nature 387:183-188.
2. Finzi D, Blankson J, Siliciano JD, Margolick JB, Chadwick K, Pierson T, Smith K, Lisziewicz J, Lori F, Flexner C. 1999. Latent infection of CD4+ T cells provides a mechanism for lifelong persistence of HIV-1, even in patients on effective combination therapy. Nature medicine 5:512-517.
3. Siliciano RF, Greene WC. 2011. HIV latency. Cold Spring Harbor perspectives in medicine 1:a007096.
4. Eisele E, Siliciano RF. 2012. Redefining the viral reservoirs that prevent HIV-1 eradication. Immunity 37:377-388.
5. Van Lint C, Bouchat S, Marcello A. 2013. HIV-1 transcription and latency: an update. Retrovirology 10:1-38.
6. Archin NM, Sung JM, Garrido C, Soriano-Sarabia N, Margolis DM. 2014. Eradicating HIV-1 infection: seeking to clear a persistent pathogen. Nature Reviews Microbiology 12:750-764.
7. Weinberger LS, Burnett JC, Toettcher JE, Arkin AP, Schaffer DV. 2005. Stochastic gene expression in a lentiviral positive-feedback loop: HIV-1 Tat fluctuations drive phenotypic diversity. Cell 122:169-182.
8. Weinberger LS, Dar RD, Simpson ML. 2008. Transient-mediated fate determination in a transcriptional circuit of HIV. Nature genetics 40:466-470.

1311 9. Razooky BS, Pai A, Aull K, Rouzine IM, Weinberger LS. 2015. A hardwired HIV
1312 latency program. Cell 160:990-1001.
1313 10. Ho Y-C, Shan L, Hosmane NN, Wang J, Laskey SB, Rosenbloom DI, Lai J, Blankson
1314 JN, Siliciano JD, Siliciano RF. 2013. Replication-competent noninduced proviruses in
1315 the latent reservoir increase barrier to HIV-1 cure. Cell 155:540-551.
1316 11. Weinberger AD, Weinberger LS. 2013. Stochastic fate selection in HIV-infected
1317 patients. Cell 155:497-499.
1318 12. Weinberger LS, Shenk T. 2006. An HIV feedback resistor: auto-regulatory circuit
1319 deactivator and noise buffer. PLoS Biol 5:e9.
1320 13. Arkin A, Ross J, McAdams HH. 1998. Stochastic kinetic analysis of developmental
1321 pathway bifurcation in phage λ-infected Escherichia coli cells. Genetics 149:1633-
1322 1648.
1323 14. Dodd IB, Perkins AJ, Tsemitsidis D, Egan JB. 2001. Octamerization of λ CI repressor
1324 is needed for effective repression of P RM and efficient switching from lysogeny.
1325 Genes & development 15:3013-3022.
1326 15. Dwarakanath RS, Clark CL, McElroy AK, Spector DH. 2001. The use of recombinant
1327 baculoviruses for sustained expression of human cytomegalovirus immediate early
1328 proteins in fibroblasts. Virology 284:297-307.
1329 16. Sanders RL, Clark CL, Morello CS, Spector DH. 2008. Development of cell lines that
1330 provide tightly controlled temporal translation of the human cytomegalovirus IE2
1331 proteins for complementation and functional analyses of growth-impaired and
1332 nonviable IE2 mutant viruses. Journal of virology 82:7059-7077.
1333 17. Stinski MF, Petrik D. 2008. Functional roles of the human cytomegalovirus essential
1334 IE86 protein, p 133-152, Human Cytomegalovirus. Springer.

1335 18. Ragoczy T, Miller G. 2001. Autostimulation of the Epstein-Barr virus BRLF1
1336 promoter is mediated through consensus Sp1 and Sp3 binding sites. Journal of
1337 virology 75:5240-5251.
1338 19. Sarisky RT, Gao Z, Lieberman PM, Fixman ED, Hayward GS, Hayward SD. 1996. A
1339 replication function associated with the activation domain of the Epstein-Barr virus
1340 Zta transactivator. Journal of virology 70:8340-8347.
1341 20. Cai W, Astor T, Liptak L, Cho C, Coen D, Schaffer P. 1993. The herpes simplex virus
1342 type 1 regulatory protein ICP0 enhances virus replication during acute infection and
1343 reactivation from latency. Journal of virology 67:7501-7512.
1344 21. Kent JR, Kang W, Miller CG, Fraser NW. 2003. Herpes simplex virus latency-
1345 associated transcript gene function. Journal of neurovirology 9:285-290.
1346 22. Roizman B, Gu H, Mandel G. 2005. The first 30 minutes in the life of a virus:
1347 unREST in the nucleus. Cell Cycle 4:1019-1021.
1348 23. Razooky BS, Weinberger LS. 2011. Mapping the architecture of the HIV-1 Tat
1349 circuit: A decision-making circuit that lacks bistability and exploits stochastic noise.
1350 Methods 53:68-77.
1351 24. Bachu M, Mukthey AB, Murali RV, Cheedarla N, Mahadevan A, Shankar SK, Satish
1352 KS, Kundu TK, Ranga U. 2012. Sequence insertions in the HIV type 1 subtype C
1353 viral promoter predominantly generate an additional NF-κB binding site. AIDS
1354 research and human retroviruses 28:1362-1368.
1355 25. Bachu M, Yalla S, Asokan M, Verma A, Neogi U, Sharma S, Murali RV, Mukthey
1356 AB, Bhatt R, Chatterjee S. 2012. Multiple NF-κB sites in HIV-1 subtype C long
1357 terminal repeat confer superior magnitude of transcription and thereby the enhanced
1358 viral predominance. Journal of Biological Chemistry 287:44714-44735.

1359 26. Burnett JC, Miller-Jensen K, Shah PS, Arkin AP, Schaffer DV. 2009. Control of
1360 stochastic gene expression by host factors at the HIV promoter. PLoS Pathog
1361 5:e1000260.
1362 27. Li X, Zhao X, Fang Y, Jiang X, Duong T, Fan C, Huang C-C, Kain SR. 1998.
1363 Generation of destabilized green fluorescent protein as a transcription reporter.
1364 Journal of Biological Chemistry 273:34970-34975.
1365 28. Banaszynski LA, Chen L-c, Maynard-Smith LA, Ooi AL, Wandless TJ. 2006. A
1366 rapid, reversible, and tunable method to regulate protein function in living cells using
1367 synthetic small molecules. Cell 126:995-1004.
1368 29. Maynard-Smith LA, Chen L-c, Banaszynski LA, Ooi AL, Wandless TJ. 2007. A
1369 directed approach for engineering conditional protein stability using biologically
1370 silent small molecules. Journal of Biological Chemistry 282:24866-24872.
1371 30. Gustafsdottir SM, Schallmeiner E, Fredriksson S, Gullberg M, Söderberg O, Jarvius
1372 M, Jarvius J, Howell M, Landegren U. 2005. Proximity ligation assays for sensitive
1373 and specific protein analyses. Analytical biochemistry 345:2-9.
1374 31. Söderberg O, Gullberg M, Jarvius M, Ridderstråle K, Leuchowius K-J, Jarvius J,
1375 Wester K, Hydbring P, Bahram F, Larsson L-G. 2006. Direct observation of
1376 individual endogenous protein complexes in situ by proximity ligation. Nature
1377 methods 3:995-1000.
1378 32. Verma A, Rajagopalan P, Lotke R, Varghese R, Selvam D, Kundu TK, Ranga U.
1379 2016. Functional incompatibility between the generic NF-κB motif and a subtype-
1380 specific Sp1III element drives the formation of the HIV-1 subtype C viral promoter.
1381 Journal of virology 90:7046-7065.
1382 33. Barbeau B, Bernier R, Dumais N, Briand G, Olivier M, Faure R, Posner BI, Tremblay
1383 M. 1997. Activation of HIV-1 long terminal repeat transcription and virus replication

via NF-κB-dependent and-independent pathways by potent phosphotyrosine phosphatase inhibitors, the peroxovanadium compounds. Journal of Biological Chemistry 272:12968-12977.

34. Chen-Park FE, Huang D-B, Noro B, Thanos D, Ghosh G. 2002. The κB DNA sequence from the HIV long terminal repeat functions as an allosteric regulator of HIV transcription. Journal of Biological Chemistry 277:24701-24708.

35. Stroud JC, Oltman A, Han A, Bates DL, Chen L. 2009. Structural basis of HIV-1 activation by NF-κB—A higher-order complex of p50: Rela bound to the HIV-1 LTR. Journal of molecular biology 393:98-112.

36. Williams SA, Chen LF, Kwon H, Ruiz□Jarabo CM, Verdin E, Greene WC. 2006. NF□κB p50 promotes HIV latency through HDAC recruitment and repression of transcriptional initiation. The EMBO journal 25:139-149.

37. Kinoshita S, Chen BK, Kaneshima H, Nolan GP. 1998. Host control of HIV-1 parasitism in T cells by the nuclear factor of activated T cells. Cell 95:595-604.

38. Kinoshita S, Su L, Amano M, Timmerman LA, Kaneshima H, Nolan GP. 1997. The T cell activation factor NF-ATc positively regulates HIV-1 replication and gene expression in T cells. Immunity 6:235-244.

39. Macián F, Rao A. 1999. Reciprocal modulatory interaction between human immunodeficiency virus type 1 Tat and transcription factor NFAT1. Molecular and Cellular Biology 19:3645-3653.

40. Southgate CD, Green MR. 1991. The HIV-1 Tat protein activates transcription from an upstream DNA-binding site: implications for Tat function. Genes & Development 5:2496-2507.

41. Dandekar DH, Ganesh KN, Mitra D. 2004. HIV□1 Tat directly binds to NFκB enhancer sequence: role in viral and cellular gene expression. Nucleic acids research 32:1270-1278.

42. Barboric M, Peterlin BM. 2005. A new paradigm in eukaryotic biology: HIV Tat and the control of transcriptional elongation. PLoS Biol 3:e76.

43. Mbonye U, Karn J. 2017. The molecular basis for human immunodeficiency virus latency. Annual review of virology 4:261-285.

44. Pierson T, McArthur J, Siliciano RF. 2000. Reservoirs for HIV-1: mechanisms for viral persistence in the presence of antiviral immune responses and antiretroviral therapy. Annual review of immunology 18:665-708.

45. Pearson R, Kim YK, Hokello J, Lassen K, Friedman J, Tyagi M, Karn J. 2008. Epigenetic silencing of human immunodeficiency virus (HIV) transcription by formation of restrictive chromatin structures at the viral long terminal repeat drives the progressive entry of HIV into latency. Journal of virology 82:12291-12303.

46. Perelson AS, Neumann AU, Markowitz M, Leonard JM, Ho DD. 1996. HIV-1 dynamics in vivo: virion clearance rate, infected cell life-span, and viral generation time. Science 271:1582-1586.

47. Van Duyne R, Easley R, Wu W, Berro R, Pedati C, Klase Z, Kehn-Hall K, Flynn EK, Symer DE, Kashanchi F. 2008. Lysine methylation of HIV-1 Tat regulates transcriptional activity of the viral LTR. Retrovirology 5:40.

48. Xie B, Invernizzi CF, Richard S, Wainberg MA. 2007. Arginine methylation of the human immunodeficiency virus type 1 Tat protein by PRMT6 negatively affects Tat Interactions with both cyclin T1 and the Tat transactivation region. Journal of virology 81:4226-4234.

1431 49. Pagans S, Kauder SE, Kaehlcke K, Sakane N, Schroeder S, Dormeyer W, Trievel RC,
1432 Verdin E, Schnolzer M, Ott M. 2010. The Cellular lysine methyltransferase Set7/9-
1433 KMT7 binds HIV-1 TAR RNA, monomethylates the viral transactivator Tat, and
1434 enhances HIV transcription. Cell host & microbe 7:234-244.
1435 50. Sivakumaran H, van der Horst A, Fulcher AJ, Apolloni A, Lin M-H, Jans DA,
1436 Harrich D. 2009. Arginine methylation increases the stability of human
1437 immunodeficiency virus type 1 Tat. Journal of virology 83:11694-11703.
1438 51. Endo-Munoz L, Warby T, Harrich D, McMillan NA. 2005. Phosphorylation of HIV
1439 Tat by PKR increases interaction with TAR RNA and enhances transcription.
1440 Virology journal 2:17.
1441 52. Ammosova T, Berro R, Jerebtsova M, Jackson A, Charles S, Klase Z, Southerland W,
1442 Gordeuk VR, Kashanchi F, Nekhai S. 2006. Phosphorylation of HIV-1 Tat by CDK2
1443 in HIV-1 transcription. Retrovirology 3:1-21.
1444 53. Brès V, Kiernan RE, Linares LK, Chable-Bessia C, Plechakova O, Tréand C, Emiliani
1445 S, Peloponese J-M, Jeang K-T, Coux O. 2003. A non-proteolytic role for ubiquitin in
1446 Tat-mediated transactivation of the HIV-1 promoter. Nature cell biology 5:754-761.
1447 54. Tosi G, Meazza R, De Lerma Barbaro A, D'Agostino A, Mazza S, Corradin G, Albini
1448 A, Noonan DM, Ferrini S, Accolla RS. 2000. Highly stable oligomerization forms of
1449 HIV□1 Tat detected by monoclonal antibodies and requirement of monomeric forms
1450 for the transactivating function on the HIV□1 LTR. European journal of immunology
1451 30:1120-1126.
1452 55. Ott M, Dorr A, Hetzer□Egger C, Kaehlcke K, Schnolzer M, Henklein P, Cole P,
1453 Zhou MM, Verdin E. Tat Acetylation: A Regulatory Switch between Early and Late
1454 Phases in HIV Transcription Elongation, p 182-196. *In* (ed), Wiley Online Library,

56. Van Zyl G, Bale MJ, Kearney MF. 2018. HIV evolution and diversity in ART-treated patients. Retrovirology 15:1-12.

57. Jeeninga RE, Hoogenkamp M, Armand-Ugon M, de Baar M, Verhoef K, Berkhout B. 2000. Functional differences between the long terminal repeat transcriptional promoters of human immunodeficiency virus type 1 subtypes A through G. Journal of virology 74:3740-3751.

58. Mbondji-Wonje C, Dong M, Wang X, Zhao J, Ragupathy V, Sanchez AM, Denny TN, Hewlett I. 2018. Distinctive variation in the U3R region of the 5'Long Terminal Repeat from diverse HIV-1 strains. PloS one 13:e0195661.

59. Montano MA, Novitsky VA, Blackard JT, Cho NL, Katzenstein DA, Essex M. 1997. Divergent transcriptional regulation among expanding human immunodeficiency virus type 1 subtypes. Journal of virology 71:8657-8665.

60. Garcia JA, Harrich D, Pearson L, Mitsuyasu R, Gaynor RB. 1988. Functional domains required for tat□induced transcriptional activation of the HIV□1 long terminal repeat. The EMBO journal 7:3143-3147.

61. Pereira LA, Bentley K, Peeters A, Churchill MJ, Deacon NJ. 2000. SURVEY AND SUMMARY A compilation of cellular transcription factor interactions with the HIV-1 LTR promoter. Nucleic acids research 28:663-668.

62. Bosque A, Planelles V. 2009. Induction of HIV-1 latency and reactivation in primary memory CD4+ T cells. Blood, The Journal of the American Society of Hematology 113:58-65.

63. Chan JK, Bhattacharyya D, Lassen KG, Ruelas D, Greene WC. 2013. Calcium/calcineurin synergizes with prostratin to promote NF-κB dependent activation of latent HIV. PLoS One 8:e77749.

64. Colin L, Van Lint C. 2009. Molecular control of HIV-1 postintegration latency: implications for the development of new therapeutic strategies. Retrovirology 6:111.

65. Duverger A, Wolschendorf F, Zhang M, Wagner F, Hatcher B, Jones J, Cron RQ, van der Sluis RM, Jeeninga RE, Berkhout B. 2013. An AP-1 binding site in the enhancer/core element of the HIV-1 promoter controls the ability of HIV-1 to establish latent infection. Journal of virology 87:2264-2277.

66. Rohr O, Marban C, Aunis D, Schaeffer E. 2003. Regulation of HIV□1 gene transcription: from lymphocytes to microglial cells. Journal of leukocyte biology 74:736-749.

67. Baeuerle PA, Baltimore D. 1989. A 65-kappaD subunit of active NF-kappaB is required for inhibition of NF-kappaB by I kappaB. Genes & development 3:1689-1698.

68. Doetzlhofer A, Rotheneder H, Lagger G, Koranda M, Kurtev V, Brosch G, Wintersberger E, Seiser C. 1999. Histone deacetylase 1 can repress transcription by binding to Sp1. Molecular and cellular biology 19:5504-5511.

69. Suzuki T, Yamamoto T, Kurabayashi M, Nagai R, Yazaki Y, Horikoshi M. 1998. Isolation and initial characterization of GBF, a novel DNA-binding zinc finger protein that binds to the GC-rich binding sites of the HIV-1 promoter. The Journal of Biochemistry 124:389-395.

70. Mahmoudi T. 2012. The BAF complex and HIV latency. Transcription 3:171-176.

71. Pessler F, Cron R. 2004. Reciprocal regulation of the nuclear factor of activated T cells and HIV-1. Genes & Immunity 5:158-167.

72. Bates DL, Barthel KK, Wu Y, Kalhor R, Stroud JC, Giffin MJ, Chen L. 2008. Crystal structure of NFAT bound to the HIV-1 LTR tandem κB enhancer element. Structure 16:684-694.

1504 73. Giffin MJ, Stroud JC, Bates DL, von Koenig KD, Hardin J, Chen L. 2003. Structure
1505 of NFAT1 bound as a dimer to the HIV-1 LTR κB element. Nature Structural &
1506 Molecular Biology 10:800-806.
1507 74. Chatterjee A, Kaznessis YN, Hu W-S. 2008. Tweaking biological switches through a
1508 better understanding of bistability behavior. Current opinion in biotechnology 19:475-
1509 481.
1510 75. Hoffmann A, Levchenko A, Scott ML, Baltimore D. 2002. The IκB-NF-κB signaling
1511 module: temporal control and selective gene activation. Science 298:1241-1245.
1512 76. Smith KA, Popmihajlov Z. 2008. The quantal theory of immunity and the
1513 interleukin□2□dependent negative feedback regulation of the immune response.
1514 Immunological reviews 224:124-140.
1515 77. Gartner MJ, Roche M, Churchill MJ, Gorry PR, Flynn JK. 2020. Understanding the
1516 mechanisms driving the spread of subtype C HIV-1. EBioMedicine 53:102682.
1517 78. Jordan A, Bisgrove D, Verdin E. 2003. HIV reproducibly establishes a latent infection
1518 after acute infection of T cells in vitro. The EMBO journal 22:1868-1877.
1519 79. Miller-Jensen K, Dey SS, Pham N, Foley JE, Arkin AP, Schaffer DV. 2012.
1520 Chromatin accessibility at the HIV LTR promoter sets a threshold for NF-κB
1521 mediated viral gene expression. Integrative Biology 4:661-671.
1522 80. Dahabieh MS, Ooms M, Brumme C, Taylor J, Harrigan PR, Simon V, Sadowski I.
1523 2014. Direct non-productive HIV-1 infection in a T-cell line is driven by cellular
1524 activation state and NFκB. Retrovirology 11:1-17.
1525 81. Li Z, Guo J, Wu Y, Zhou Q. 2013. The BET bromodomain inhibitor JQ1 activates
1526 HIV latency through antagonizing Brd4 inhibition of Tat-transactivation. Nucleic
1527 acids research 41:277-287.

1528 82. Jordan M, Schallhorn A, Wurm FM. 1996. Transfecting mammalian cells:
1529 optimization of critical parameters affecting calcium-phosphate precipitate formation.
1530 Nucleic acids research 24:596-601.
1531 83. Zhu H, Coppinger JA, Jang C-Y, Yates III JR, Fang G. 2008. FAM29A promotes
1532 microtubule amplification via recruitment of the NEDD1–γ-tubulin complex to the
1533 mitotic spindle. The Journal of cell biology 183:835-848.

1534

1535 **Table 1: Primer sets used in PCR**

1536

Primer sets used for the site-directed mutagenesis of NF-κB copy-number variant LTRs in the pcLGIT/pcLdGIT vector (ATF model)			
LTR-Variant	**Primer pair**	**Description**	**Sequence of primers (5'-3')**
FHHC (4-κB)	N1992 FP	Inner primers	TGACACAGAAGGGACTTTCTGCTGACAC AGAAGGGACTTTCCGCTGGGACTTTCCAC TGGGGCGTTCC
	N1993 RP		AAGTCCCAGCGGAAAGTCCCTTCTGTGTC AGCAGAAAGTCCCTTCTGTGTCAGCAGTC TTTGTAAAACTCCG
OHHC (3-κB)	N1994 FP		TGACACAGAATCTACTTTTTGCTGACACA GAAGGGACTTTCCGCTGGGACTTTCCACT GGGGCGTTCC
	N1995 RP		AAGTCCCAGCGGAAAGTCCCTTCTGTGTC AGCAAAAAGTAGATTCTGTGTCAGCAGT CTTTGTAAAACTCCG
OOHC (2-κB)	N1996 FP		TGACACAGAATCTACTTTTTGCTGACACA GAATCTACTTTTTGCTGGGACTTTCCACT GGGGCGTTCC
	N1997 RP		AAGTCCCAGCAAAAAGTAGATTCTGTGT CAGCAAAAAGTAGATTCTGTGTCAGCAG TCTTTGTAAAACTCCG
OOOC (1-κB)	N1998 FP		TGACACAGAATCTACTTTTTGCTGACACA GAATCTACTTTTTGCTTCTACTTTTTACTG

	N1999 RP		GGGCGTTCC AAGTAGAAGCAAAAAGTAGATTCTGTGT CAGCAAAAAGTAGATTCTGTGTCAGCAG TCTTTGTAAAACTCCG
OOOO (0-κB)	N2000 FP N2001 RP		TGACACAGAATCTACTTTTTGCTGACACA GAATCTACTTTTTGCTTCTACTTTTTACTT CTACTTTTTAGG AAGTAGAAGCAAAAAGTAGATTCTGTGT CAGCAAAAAGTAGATTCTGTGTCAGCAG TCTTTGTAAAACTCCG

Primers used for the construction of the pcLdGITRD vector backbone (p913 series; TTF model)

Amplicon	Amplicon length	Primer pair	Sequence of primers (5'- 3')
d2EGFP-IRES-Tat	1779 bp	N2720 FP N2724 RP	TTTCTTCCATTGCGGCCGCGCCGCCACCA TGGCCTCCTCCGAGAACGTC GGCCATTTCGAAGTCGAAGGGGTCT
DsRed2-RFP	629 bp	N2723 FP N2726 RP	ACTTCGAAATGGCCTCCTCCGAGAACG TCCGATATCCAGGAACAGGTGGTGGC
FKBP DD	353 bp	N2725 FP N2722 RP	TGTTCCTGGATATCGGAGTGCAGGTGGA AACCATC CGTACGCGGCGCGCCTCATTCCAGTTCTA GAAGCTCC

Primers used for the determination of proviral integration frequency

Target region	Primer pair/ primer-probe combination	Primer/probe sequence (5'-3')
Strong-stop DNA	N2208 FP N2209 RP N2210 probe	GATCTGAGCC(T/C)GGGAGCTCTCTG TCTGAGGGATCTCTAGTTACCAGAGTC FAM-CTGCTTAAGCCTCAATAAAGCTTGCCTTGAGTGC T-TAMRA

Primers used in Chromatin immunoprecipitation- qPCR

LTR-enhancer	N2493 FP N2215 RP N2492 probe	CCGGAGT(A/T)TTACAAAGACTGCTG CTGCTTATATGCAGCATCTGAGG HEX-CACTGGGGCGTTCCAGG(G/A)GG(A/T)GT-BHQ

Figure legends

Figure 1: A schematic representation of NF-κB motif diversity in HIV-1C LTR. The canonical HIV-1B LTR containing two identical NF-κB motifs is presented at the top. The distinct regulatory regions (U3, R, U5, the modulator, the enhancer, and the core promoter) and important transcription factor binding sites have been depicted. HIV-1C LTR not only contains more copies of the NF-κB motif (3 or 4 copies) but the additional motifs are also genetically variable (the bottom panel). The three genetically distinct NF-κB motifs present in the C-LTR are denoted as H (GGGACTTTCC), C (GGGGCGTTCC, differences underlined), and F (GGGACTTTCT). Note that the Sp1III site also contains subtype-specific variations as presented; B and C representing respective viral subtypes.

Figure 2: Viral gene expression is proportional to the number of NF-κB motifs in the C-LTR. (A) A schematic of the cLGIT/cLdGIT sub-genomic viral vector panels of the autonomous feedback (ATF) model is presented. Note that both the 3' LTR and Tat are of HIV-1C origin. The nucleotide sequences of the four NF-κB motifs and the inactivating mutations introduced in the motifs of the variant viral strains have been depicted. The EGFP

reporter gene (half-life ~ 48 h) of the cLGIT vector backbone is replaced with its shorter half-life variant d2EGFP (half-life ~ 2h) in the cLdGIT backbone. **(B)** The time schematic of the gene-expression analysis from the cLGIT vector panel. One million Jurkat cells were infected at an RIU of ~ 0.5-0.6, independently with each LTR-variant strain. After 72 h of infection, half of the infected cells were activated with a cocktail of global T-cell activators (PMA+TNFα+TSA+HMBA) and 24 h post-activation, EGFP and Tat-transcript expressions were estimated for both the un-activated and activated fractions using a flow-cytometer and a Tat specific RT-PCR, respectively. **(C)** Representative EGFP histograms of the five variant LTRs. The black dotted histogram represents Jurkat cells not infected and not activated; the black hollow histogram represents cells infected but not activated, and the solid grey histogram represents cells infected and activated. The intensity ranges of $EGFP^{-}$, $EGFP^{Low}$, and $EGFP^{High}$ are indicated as GFP^{-}, GFP^{L} and GFP^{H}, respectively along with the frequency of each fraction (% values). The black arrows point at the gradual decline in the $EGFP^{High}$ (MFI > 10^4 RFU) population representing the Tat-transactivated population with decreasing copies of NF-κB elements. **(D)** The mean EGFP MFI values from experimental quadruplicates ± SD, data are representative of two independent experiments. Two-way ANOVA with Bonferroni post-test correction was used for the statistical evaluation (*$p<0.05$, ***$p<0.001$ and ns – non-significant). The % GFP^{+} profile in the inset confirms near equivalent infection of the target cells with the LTR-variant viral strains at ~ 0.5-0.6 RIU. **(E)** EGFP-expression manifests a positive linear correlation with the NF-κB copy-number as indicated by the fold enhancement in the EGFP MFI (ratio of the EGFP MFI values of the activated and uninduced fractions from each variant LTR) vs NF-κB copy-number plot. **(F)** Live-dead assay to compare the % live cells between the activated and uninduced pairs. Mean values from experimental quadruplicates ± SD, data are representative of two independent experiments (*$p<0.05$, ns- non significant; two-tailed, unpaired *t*-test). **(G)** Tat expression

was evaluated in an RT-PCR using the ΔΔCt method and GAPDH as the reference gene from total mRNA extracted from 0.2 to 0.5 million cells of un-activated and activated populations. Mean values of the relative Tat-mRNA expression from three independent experiments ± SEM are plotted. Two-way ANOVA with Bonferroni post-test correction was used for statistical analyses. (**p<0.01, ***p<0.001 and ns – non-significant). **(H)** The Tat transcript expression is directly proportional to the NF-κB copy number as observed from the fold enhancement in the Tat transcript levels of the activated fraction over the uninduced fraction. **(I)** Comparable GAPDH Ct values for the different stimulation conditions as well as across the variant viral strains are indicated (*p<0.05, ns- non significant; two-tailed, unpaired *t*-test).

Figure 3: In the ATF model, the stronger the promoter, the faster the latency establishment. (A) A schematic representation of the experimental protocol is depicted. One million Jurkat cells were infected with individual strains of the cLGIT panel at a low infectious titer of ~0.1-0.2 RIU, allowed to relax for a week, treated with the cocktail of global T-cell activators, and 24 h later, all the $EGFP^{+}$ cells (harboring active provirus; MFI $>10^{3}$ RFU) were sorted. The sorted, total $EGFP^{+}$ cells were then maintained in culture, and the EGFP expression was monitored by flow cytometry every four days and that of Tat transcripts on days 0, 8 and 16. **(B)** The gating strategies used to sort the total $EGFP^{+}$ population and for the subsequent latency establishment assay are depicted. Initially, the debris were excluded in the FSC vs SSC scatter plot, and the total $EGFP^{+}$ cells from the population- P were sorted. Importantly, a live-dead exclusion dye was used to stain the post-sorted cells to include only the live, $EGFP^{+}$ for the latency kinetics analyses. The total $EGFP^{+}$ gate was further sub-gated into $EGFP^{Low}$ and $EGFP^{High}$ fractions for subsequent analyses (Figure 3F and 3G, respectively). **(C)** Representative, post-sort, stacked histograms

representing the temporal events during transcriptional silencing. The NF-κB variant viral strains demonstrate varying proportions of $EGFP^{High}$ and $EGFP^{Low}$ cells in the total $EGFP^{+}$ sort. **(D), (E), (F),** and **(G)** indicate the kinetic curves corresponding to the total EGFP MFI, percentages of total $EGFP^{+}$, $EGFP^{High}$, and $EGFP^{Low}$ cells, respectively. Data are representative of three independent experiments. Mean values from experimental triplicates ± SD, are plotted. Two-way ANOVA with Bonferroni post-test correction was used for the statistical evaluation (***$p<0.001$). **(H)** Kinetic curves of relative Tat-mRNA levels of the NF-κB variant strains **(I)** The absolute Ct values of the GAPDH transcripts at different time points. Data are representative of two independent experiments. Mean values from experimental triplicates ± SD plotted. Two-way ANOVA with Bonferroni post-test correction was used for the statistical evaluation (***$p<0.001$). **(J)** The integration frequency for the five LTR-variant viral strains was estimated using the standard curve and the regression analysis. Viral integration was found to be ~1.0 per cell for all the five variants. Data are representative of two independent experiments. Mean values from experimental triplicates ± SD values are plotted. **(K)** Live-dead analysis confirms comparable levels of % live cells between the NF-κB variants and across different time-points.

Figure 4: The binary latency trajectory of the GFP^{High} population delineates the viral promoter into strong (3- and 4-κB) and weak (2, 1, and 0-κB) LTRs. **(A)** The experimental schemes to study the kinetics of latency establishment in $EGFP^{High}$ and $d2EGFP^{High}$ cells **(B), (C), (D)** and **(E)** represent the comparative kinetic profiles of EGFP MFI, % $EGFP^{+}$, d2EGFP MFI and % $d2EGFP^{+}$ cells, respectively. Mean values from experimental triplicates ± SD, representative of two independent experiments are plotted. Two-way ANOVA with Bonferroni post-test correction was used for the statistical evaluation

(***p<0.001 and ns – non-significant). **(F)** The stacked histogram profiles of the $EGFP^{High}$ cells during latency establishment is presented. The sorted $EGFP^{High}$ cells (GFP^{H}; MFI $>10^4$ RFU) comprising of a homogeneous population of Tat-mediated transactivated cells, transitioned to the $EGFP^{-}$ phenotype (GFP^{-}) through an $EGFP^{Low}$ cluster (GFP^{L}; MFI $\sim10^2$ – 10^4 RFU) representing the cells with a basal-level transcription without an intermediate phenotype. **(G)** The stacked histogram profile of the $d2EGFP^{High}$ cells during latency establishment identified regions of $d2EGFP^{-}$ (GFP^{-}; MFI $<10^3$ RFU), $d2EGFP^{Low}$ (GFP^{L}; MFI $\sim10^3$–10^4 RFU), and $d2EGFP^{High}$ (GFP^{H}; MFI $>10^4$ RFU) phenotypes as demarcated. Of note, given the shorter half-life of d2EGFP, the stability of the $d2EGFP^{Low}$ phenotype was extremely transient; hence the present system lacked a distinct $d2EGFP^{Low}$ cluster at any time point unlike in the EGFP system (Figures 3C and 4G).

Figure 5: The manifestation of three distinct latency phenotypes of single $EGFP^{High}$ cells. (A) The experimental layout of latency establishment in single-cell clones is essentially similar to that of the non-clonal, population kinetics as in Figure 4A. The $EGFP^{High}$ cells (MFI $>10^4$ RFU) were single-cell sorted, expanded for three-four weeks, and the pattern of EGFP expression was assessed on days 21 and 28 post-sorting by flow cytometry and fluorescence microscopy. EGFP expression of 16 randomly selected clones, corresponding to each viral variant was measured. **(B)** Based on the fluorescence profile, three distinct categories of clone- persisters ($EGFP^{High}$, MFI $>10^4$ RFU), relaxers ($EGFP^{-}$, MFI $<10^3$), and bimodallers (binary population of persisters and relaxers) were identified. **(C)** The relative proportion of the above three phenotypes among the LTR-variants as a function of time as indicated at Day 21 and 28 post-sorting. **(D)** and **(H)** Two bimodal cell lines, 3c and 8c representing the 4-κB and 3-κB LTRs, respectively, demonstrate bimodal gene expression. The sorted $EGFP^{-}$ cells from the 4-κB and 3-κB clones generate 95.8% (Figure 5D) and

90.4% (Figure 5H) EGFP^{High} cells, respectively, following activation with the global activation cocktail with negligible proportion of cells displaying the intermediate phenotype. **(E)** and **(I)** A Taqman qPCR targeting a region of the LTR, performed as in Figure 3J, confirms a comparable integration frequency (~1.0 provirus per cell) between the EGFP^{-} and EGFP^{High} fractions in both the 4-κB (Figure 5E) and the 3-κB (Figure 5I) clones. **(F)** and **(J)** A quantitative real-time PCR for the Tat-transcripts demonstrated significantly higher levels of Tat-transcripts in the EGFP^{High} fraction compared to that in the EGFP^{-} fraction for both the clones. Mean values from three independent experiments ± SEM are plotted. A two-tailed, unpaired *t*-test was used for the statistical evaluation. **(G)** and **(K)** DNA cell-cycle analysis was performed on the EGFP^{-} and EGFP^{High} sub-fractions of the 4-κB (Figure 5G) and the 3-κB **(**Figure 5K) clones following the standard PI-staining protocol. The overlay histograms for the two subfractions showing the G1, S and G2/M phases are presented. The proportions of cells in the G1, S and G2/M stages were calculated for both the subfractions and depicted in the inset. Mean values from triplicates, representative of two independent reactions ± SD are plotted. A two-tailed, unpaired *t*-test was used for the statistical evaluation.

Figure 6: In the tunable Tat-feedback (TTF) model, the stronger the LTR-Tat feedback, the higher the viral gene expression. (A) A schematic of the sub-genomic HIV-1 vector backbone- cLdGITRD representing the TTF model. The 3- and 1-κB LTRs representing a strong and a weak promoter, respectively, have been used in the present study. The small molecule Shield1 stabilizes the 'Tat:RFP:DD' cassette in a dose-dependent fashion making it available for the subsequent transactivation events at the LTR. **(B)** Validation of Shield1 dose-dependent stabilization of the 'Tat:RFP:DD' cassette in HEK293T cells. One mg of the cLdGITRD-3-κB vector was transfected into 0.6 million HEK293T cells in separate wells in

the presence of varying concentrations of Shield1 as indicated, and the images were captured 48 h post-transfection. The experiment was repeated twice with comparable results. **(C)** The experimental layout to confirm Shield1 dose-dependent gene expression and Tat-transactivation in Jurkat cells is presented. Approximately 0.3 million Jurkat cells were infected with the LdGITRD-3-κB strain (20 ng/ml p24 equivalent), and post 24 h, the infected cells were split into four fractions, each treated with a different concentration of Shield1 as indicated. After 48 h of Shield1 treatment, half of the cells from each fraction were activated for 24 h followed by the quantitation of d2EGFP and Tat-mRNA expression levels for both the induced and uninduced fractions. **(D)** Representative stacked histograms indicate a Shield1 dose- dependent Tat-transactivated population (black arrows) at a fixed LTR-strength (fixed number of NF-κB motifs). The peak-height of the d2EGFP^{High} population (MFI > 10^4 MFU) proportionally reduced with the Shield1 dose; the TTF model thus confirmed the d2EGFP^{High} cluster to represent the Tat-transactivated population. **(E)** The Shield1 concentration dependent d2EGFP MFI, **(F)** fold d2EGFP enhancement, and **(G)** % d2EGFP^{+} plots are presented. Values from experimental triplicates ± SD, representing two independent experiments are plotted. Two-way ANOVA with Bonferroni post-test correction was used for the statistical evaluation (**p<0.01, ***p<0.001 and ns – non-significant). **(H)** Relative Tat-transcript levels and **(I)** fold Tat-mediated transactivation were evaluated as in Figures 2G and 2H, respectively. The mean values from three independent experiments ± SEM are plotted. Two-way ANOVA with Bonferroni post-test correction was used for the statistical evaluation (*p<0.05, ***p<0.001 and ns – non-significant).

Figure 7: The TTF model identifies two distinct modes of latency establishment in the strong and the weak LTRs. (A) The experimental scheme to study latency establishment as described in Figure 4A with slight modifications. The sorted d2EGFP^{High} cells were divided

into four separate fractions and maintained at different concentrations of Shield1 as depicted. The cells were analyzed every 24 h for d2EGFP and Tat-RFP expression using flow cytometry. **(B)** The temporal d2EGFP and Tat-RFP trajectories for the strong (3-κB; upper panel) and the weak (1-κB; lower panel) LTRs at the 3 μM Shield1 concentration are presented. The black-solid and the black-dotted arrows denote the dominant and the less dominant routes of transit for each LTR-variant, respectively. Individual kinetic curves of the four distinct populations- **(C)** % d2EGFP^{+} Tat-RFP^{-}, **(D)** % d2EGFP^{+} Tat-RFP^{+}, **(E)** % d2EGFP^{-} Tat-RFP^{+}, and **(F)** % d2EGFP^{-} Tat-RFP^{-}. Mean values from experimental triplicates ± SD are plotted. Data represent three independent experiments. Two-way ANOVA with Bonferroni post-test was used for the statistical evaluation (*$p<0.05$, ***$p<0.001$ and ns - non-significant). The solid- and dotted-coloured curves represent various concentrations of Shield1 for the 3-κB and the 1-κB LTRs, respectively.

Figure 8: Persistent presence of Tat in latent cells. (A) The temporal profile of Tat expression during LTR-silencing in a stable J-LdGIT-3-κB cell pool of the ATF model. The experimental strategy of latency establishment was similar as in Figure 4A. At defined time points, a small fraction of the sorted d2EGFP^{High} cells was flow-analyzed for d2EGFP expression (left panel), while the remaining cells were subjected to indirect immunofluorescence of Tat using a rabbit anti-Tat primary antibody and an anti-rabbit Alexa-568 conjugated secondary antibody. DAPI was used to stain the nucleus. Representative confocal images of Tat and d2EGFP-expression at indicated time points (right panel) are presented. Appropriate negative controls for Tat IF are presented in the bottom panels. The white dotted line demarcates the nucleus from the extra-nuclear compartment in each cell. Scale bar = 20 μM. **(B)** The quantitative analysis of d2EGFP and Tat-Alexa 568 intensity

levels in the nuclear and extra-nuclear compartments (arbitrary units) at multiple time points. Data from 150 individual cells at each time point and three independent experiments are presented. The threshold values for total cellular d2EGFP and Tat-Alexa 568 intensities were obtained from uninfected Jurkat cells (Figure 8A; Lane-8) and infected, unstained cells (Fig 8A; Lane-6), respectively. Mean values ± SEM are plotted. One-way ANOVA was used for statistical evaluation (***p<0.001).

Figure 9: The presence of Tat in latent cells as confirmed by the highly sensitive proximity ligation assay (PLA). (A) The detection of exogeneous B-Tat in PLA. Approximately 0.5 million HEK293T cells seeded per well in a 12-well culture dish were transfected with 800 ng of pLGIT, an expression vector encoding Tat of HIV-1B, on poly-L-lysine coated coverslips. Tat-PLA was performed according to the manufacturer's protocol using a pair of anti-Tat primary antibodies (rabbit-polyclonal; # ab43014, Abcam and mouse-monoclonal; # 7377, NIH-AIDS reagents program). Representative confocal images of a 'no antibody' control (Lane 1), single anti-Tat antibody controls (Lanes 2 and 3) and both the antibodies (Lane 4) are presented. The mean values from three independent experiments ± SEM are plotted. A one-way ANOVA with Bonferroni's multiple comparison post-test was used for statistical analyses (***p<0.001). **(B)** A DNA dose-response of PLA using pcLGIT, an expression vector encoding Tat of HIV-1C (200, 400, 800 ng). The mean GFP intensities and the average number of PLA dots per cell for the amount of pcLGIT vector transfected are presented. **(C)** The Tat PLA dot quantitation in the active vs. latent cells was performed in HEK293 cells independently and stably infected with the cLdGIT-4-κB and 3-κB strains of the ATF panel (Figure 2A). Cells were infected with one of the viral strains (~ 0.5 RIU), $d2EGFP^{High}$ cells were sorted, the cells were incubated for proviral-LTR relaxation to arrive at a mixed population of $d2EGFP^{+}$ (active) and $d2EGFP^{-}$ (latent) cells, and both the cell

1754 populations were subjected to Tat-PLA. Approximately 50,000 mixed d2EGFP cells seeded
1755 in a well of an 8-well slide chamber were subjected to PLA. Representative confocal images
1756 depicting single antibody controls (Lanes-1 and 2) and Tat-PLA with both the antibodies
1757 (Lanes-3 and 4) are shown (left panel). Two sub-fields with distinct Tat-PLA dots (white) in
1758 both d2EGFP^{+} and d2GFP^{-} cells have been enlarged for clarity. The number of Tat-PLA dots
1759 per cell was determined independently for d2EGFP^{+} as well as d2EGFP^{-} cells, and the mean
1760 values from three independent experiments ± SEM are plotted. The total number of cells
1761 counted for d2EGFP^{+} phenotype was 164 (128 for 4-κB and 36 for 3-κB) and for d2EGFP^{-}
1762 phenotype was 168 (123 for 4-κB and 45 for 3-κB). A two-tailed, unpaired *t*-test was used for
1763 statistical analyses.

1764

1765 **Figure 10: The active and latent LTRs recruit host-factors differentially. (A)** Schematic
1766 representation of the LTR sequence and the positions of the primer pairs used in the
1767 conventional PCR (240 bp, solid-black) and qPCR (127 bp, dotted black) for the ChIP
1768 analysis is depicted. **(B)** and **(E)** The pre-sort percentages of the EGFP^{-} and EGFP^{High} cells
1769 corresponding to the 4-κB (Panel-B) and the 3-κB (Panel-E) bimodal clones are presented.
1770 **(C)** and **(F)** Data from a conventional PCR-based ChIP assay of the active (EGFP^{High}) and
1771 latent (EGFP^{-}) promoters for several host factors and Tat protein are presented for the 4-κB
1772 (Panel-C) and 3-κB (Panel-F) clones, respectively. Cell-lysate from two million cells (active
1773 or latent) and 2 μg of the respective antibody were used for the individual IP reactions. A
1774 rabbit polyclonal anti-Tat antibody (# ab43014, Abcam) was used for the Tat-IP. One-tenth
1775 of the IP chromatin was used as the input control. Conventional PCR was repeated thrice for
1776 each IP reaction. Representative gel image and the corresponding densitometry analyses are
1777 presented. Data for each band are normalized to the input. The mean values from

quadruplicates ± SD are plotted. A two-tailed, unpaired *t*-test was used for statistical analyses (*p<0.05, **p<0.01, ***p<0.001, and ns- non-significant). A qPCR-based ChIP assay was performed independently using identical experimental conditions and **(D)** the 4-κB or **(G)** the 3-κB clones. The data for each IP was calculated using the percent-input method. The mean values from qPCR triplicates ± SD are plotted. A two-tailed, unpaired *t*-test was used for statistical analyses (*p<0.05, **p<0.01, ***p<0.001, and ns- non-significant). **(H)** Two additional qPCR-based ChIP assays using two different mouse monoclonal anti-Tat antibodies (1D9 and NT3 5A5.3) were performed using the active and latent fractions of the two bimodal clones. The mean values from qPCR triplicates ± SD are plotted. A two-tailed, unpaired *t*-test was used for statistical analyses (*p<0.05, **p<0.01, ***p<0.001, and ns- non-significant).

Figure 11: A hypothetical model depicting a concentration-dependent switch of the Tat protein through differential PTM(s) that mutually serve as an activator or suppressor at different phases of viral transcription. The model suggests that the diverse PTM(s) of Tat play a critical role in permitting the transactivator to toggle between being an activator or suppressor of transactivation of the LTR. At the time of commitment to latency, the intracellular concentrations of Tat are not limiting. Tat may initiate a negative feedback response of viral transcription in a concentration-dependent manner by regulating the expression of host factors that control the PTM(s) of Tat. The negative feedback effect of Tat, therefore, follows its initial positive feedback on the viral promoter. A viral promoter characterized by stronger transcriptional activity, thus, mediates the establishment of latency at a faster rate by producing more quantities of Tat. The data presented in this work are consistent with this model.

1802

1803

Figure 1

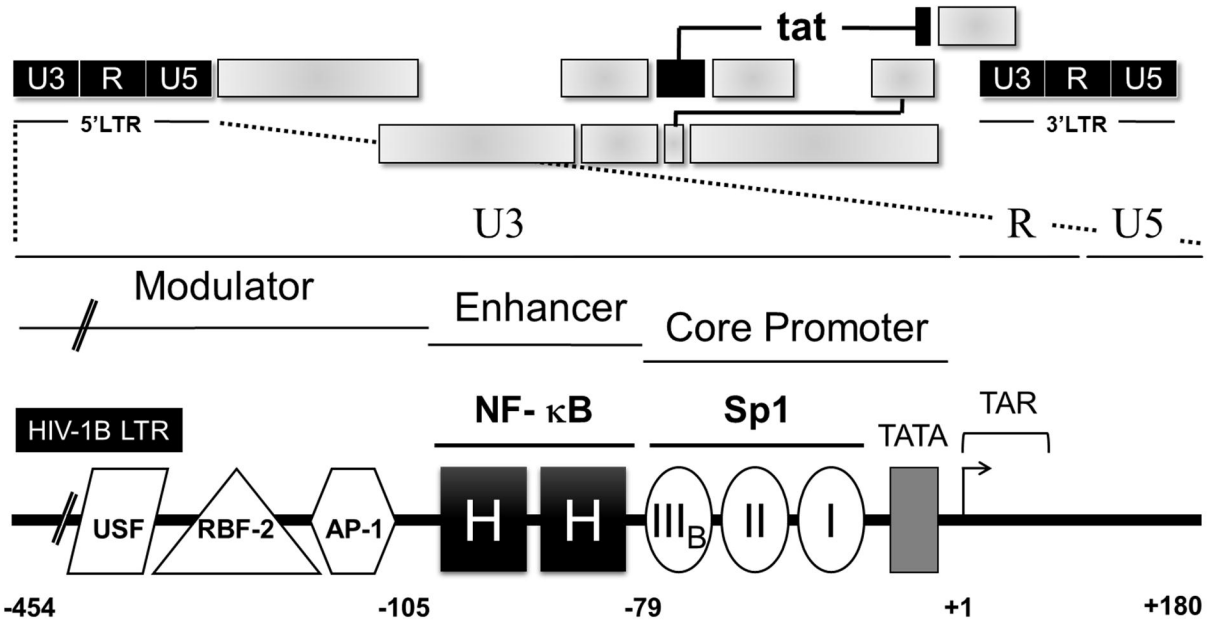
tat
U3
R
U5
5'LTR
3'LTR
U3
R
U5
Modulator
Enhancer
Core Promoter
HIV-1B LTR
NF- κB
Sp1
TATA
TAR
USF
RBF-2
AP-1
H
H
III$_B$
II
I
-454
-105
-79
+1
+180

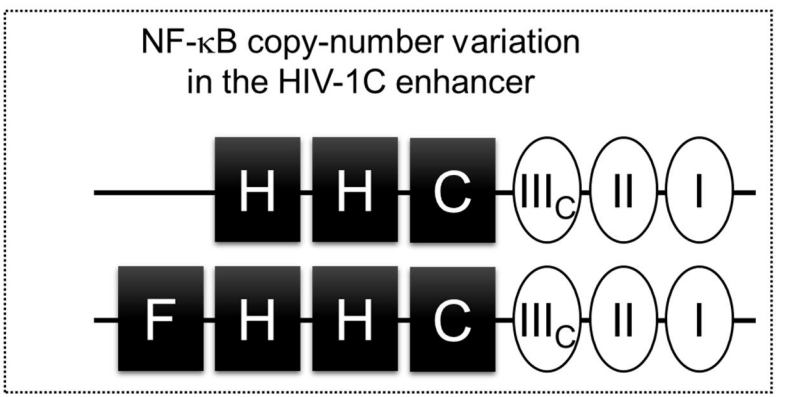
NF-κB copy-number variation
in the HIV-1C enhancer
H
H
C
III$_C$
II
I
F
H
H
C
III$_C$
II
I

Figure 2

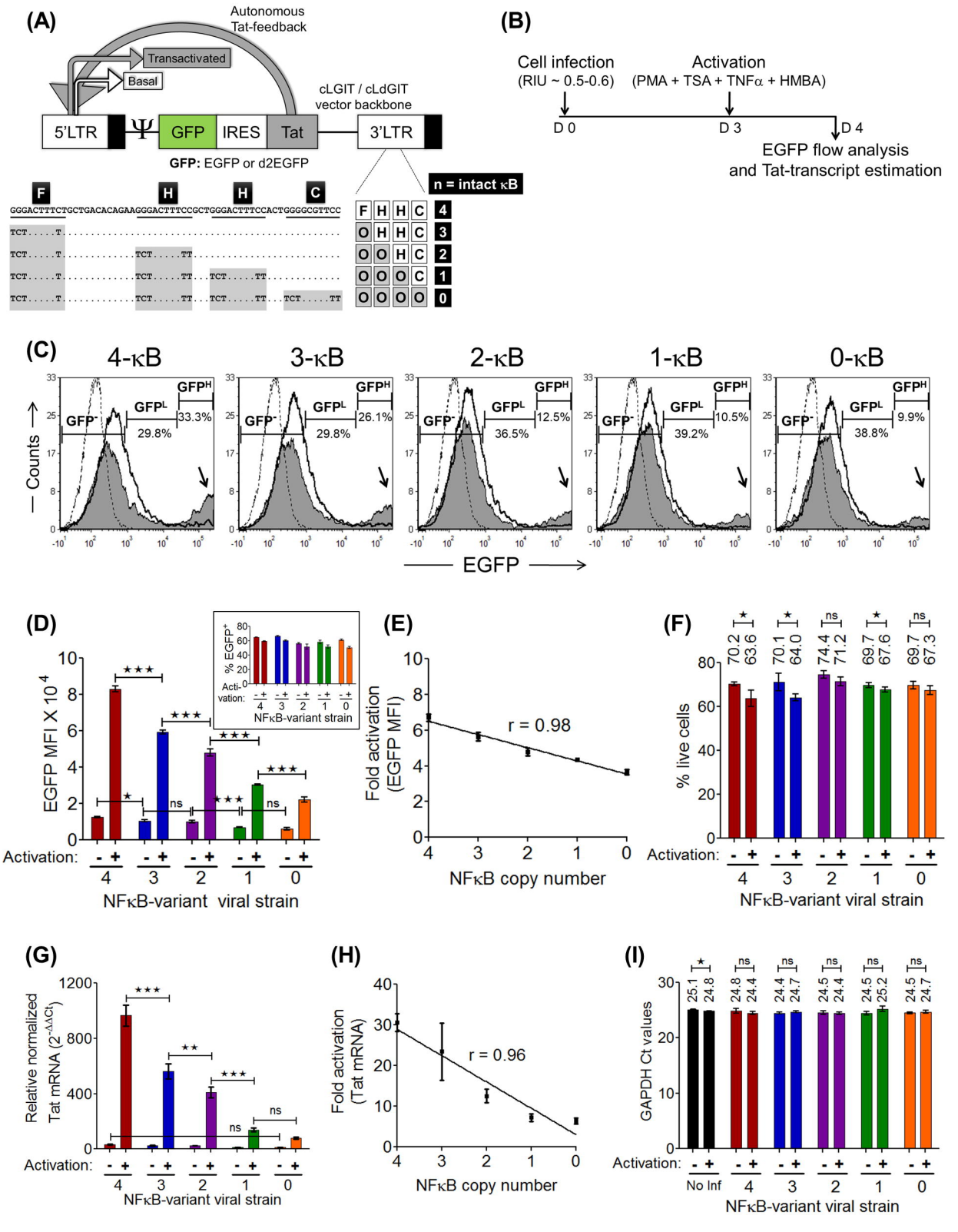
(A)
Autonomous
Tat-feedback
Transactivated
Basal
cLGIT / cLdGIT
vector backbone
5'LTR
Ψ
GFP
IRES
Tat
3'LTR
GFP: EGFP or d2EGFP
F
H
H
C
n = intact κB
GGGACTTTCTGCTGACACAGAAGGGACTTTCCGCTGGGACTTTCCACTGGGGCGTTCC
(B)
Cell infection
(RIU ~ 0.5-0.6)
Activation
(PMA + TSA + TNFα + HMBA)
D 0
D 3
D 4
EGFP flow analysis
and Tat-transcript estimation
(C)
4-κB
3-κB
2-κB
1-κB
0-κB
Counts
GFP-
GFPL
GFPH
29.8%
33.3%
29.8%
26.1%
36.5%
12.5%
39.2%
10.5%
38.8%
9.9%
EGFP
(D)
EGFP MFI X 10 4
% EGFP+
Activation:
NFκB-variant viral strain
(E)
Fold activation
(EGFP MFI)
r = 0.98
NFκB copy number
(F)
% live cells
70.2
63.6
70.1
64.0
74.4
71.2
69.7
67.6
69.7
67.3
Activation:
NFκB-variant viral strain
(G)
Relative normalized
Tat mRNA (2-ΔΔCt)
Activation:
NFκB-variant viral strain
(H)
Fold activation
(Tat mRNA)
r = 0.96
NFκB copy number
(I)
GAPDH Ct values
25.1
24.8
24.8
24.4
24.4
24.7
24.5
24.4
24.5
25.2
24.5
24.7
Activation:
No Inf
NFκB-variant viral strain

Figure 3

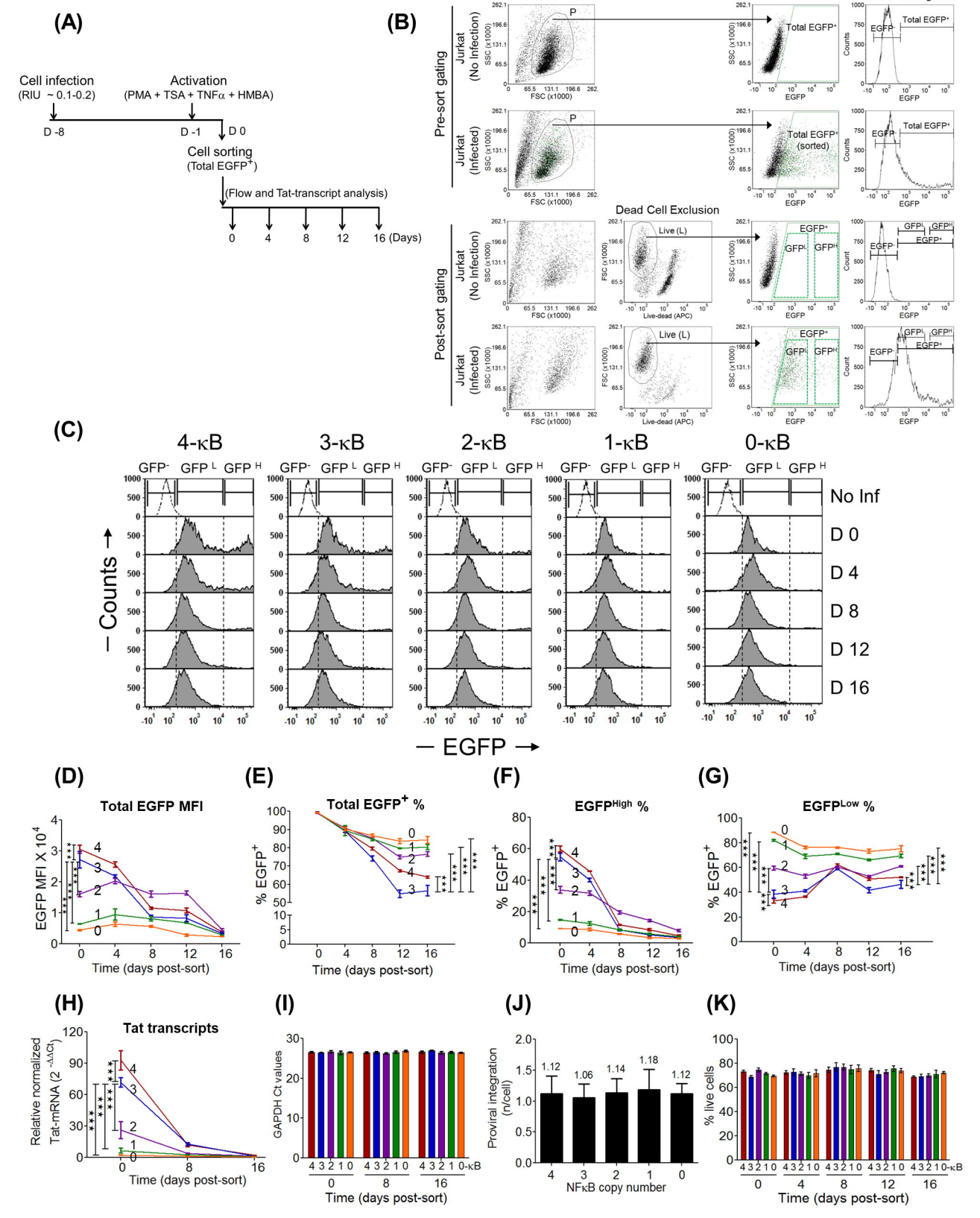
(A)
Cell infection
(RIU ~ 0.1-0.2)
Activation
(PMA + TSA + TNFα + HMBA)
D -8
D -1
D 0
Cell sorting
(Total EGFP+)
(Flow and Tat-transcript analysis)
0
4
8
12
16 (Days)
(B)
FSC vs SSC
EGFP vs SSC
EGFP histogram
Pre-sort gating
Jurkat (No Infection)
Jurkat (Infected)
Total EGFP+
Total EGFP+ (sorted)
Dead Cell Exclusion
Post-sort gating
Live (L)
Live-dead (APC)
(C)
4-κB
3-κB
2-κB
1-κB
0-κB
GFP- GFP L GFP H
No Inf
D 0
D 4
D 8
D 12
D 16
— Counts →
— EGFP →
(D)
Total EGFP MFI
EGFP MFI X 10^4
Time (days post-sort)
(E)
Total EGFP+ %
% EGFP+
(F)
EGFPHigh %
(G)
EGFPLow %
(H)
Tat transcripts
Relative normalized Tat-mRNA (2^-ΔΔCt)
(I)
GAPDH Ct values
(J)
Proviral integration (n/cell)
1.12
1.06
1.14
1.18
1.12
NFκB copy number
(K)
% live cells

Figure 4

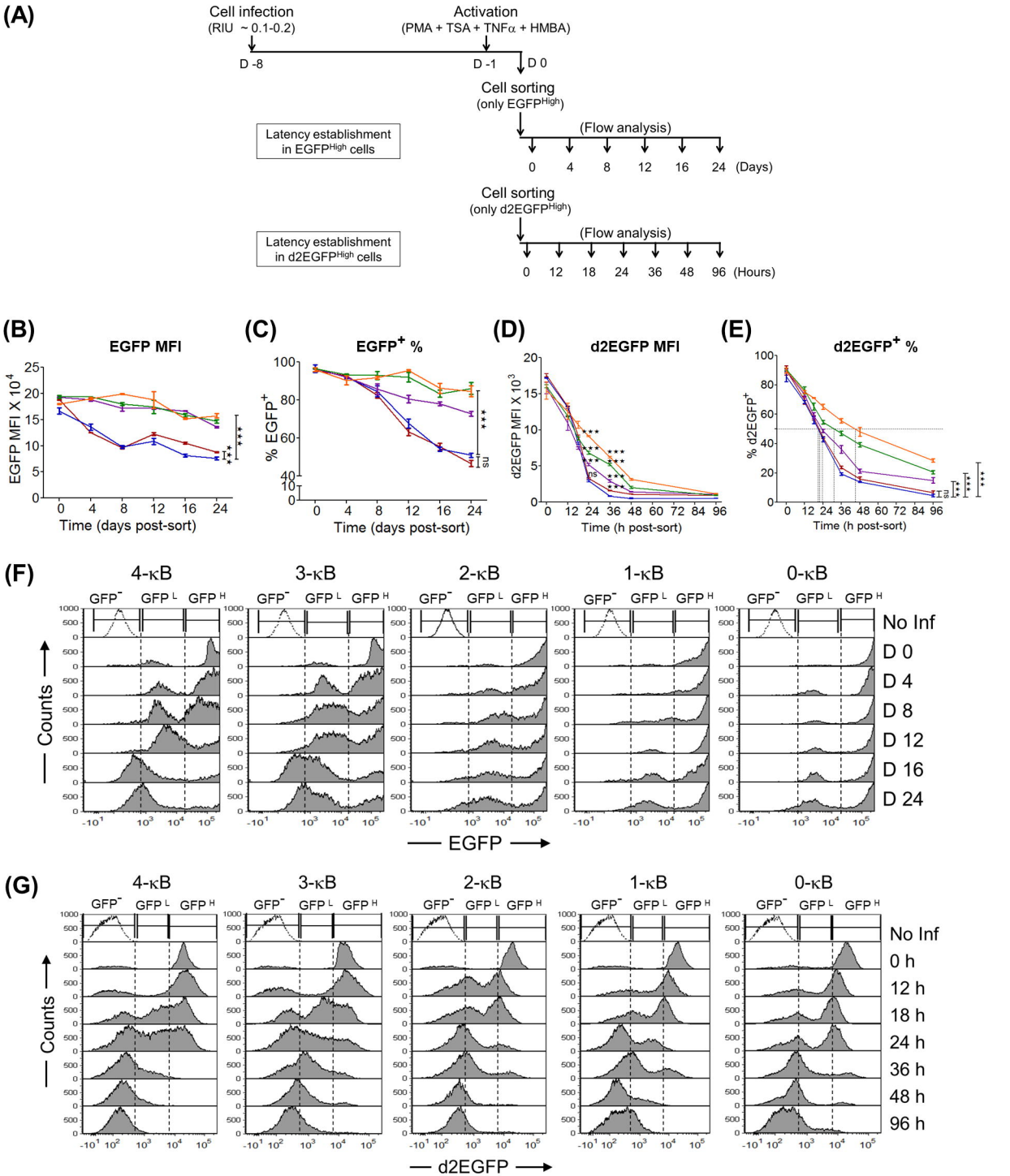
(A)
Cell infection
(RIU ~ 0.1-0.2)
Activation
(PMA + TSA + TNFα + HMBA)
D -8
D -1
D 0
Cell sorting
(only EGFP^High)
Latency establishment in EGFP^High cells
(Flow analysis)
0 4 8 12 16 24 (Days)
Cell sorting
(only d2EGFP^High)
Latency establishment in d2EGFP^High cells
(Flow analysis)
0 12 18 24 36 48 96 (Hours)
(B)
EGFP MFI
EGFP MFI X 10^4
Time (days post-sort)
(C)
EGFP+ %
% EGFP+
Time (days post-sort)
(D)
d2EGFP MFI
d2EGFP MFI X 10^3
Time (h post-sort)
(E)
d2EGFP+ %
% d2EGFP+
Time (h post-sort)
(F)
4-κB
3-κB
2-κB
1-κB
0-κB
GFP- GFP L GFP H
No Inf
D 0
D 4
D 8
D 12
D 16
D 24
Counts
EGFP
(G)
4-κB
3-κB
2-κB
1-κB
0-κB
GFP- GFP L GFP H
No Inf
0 h
12 h
18 h
24 h
36 h
48 h
96 h
Counts
d2EGFP

Figure 5

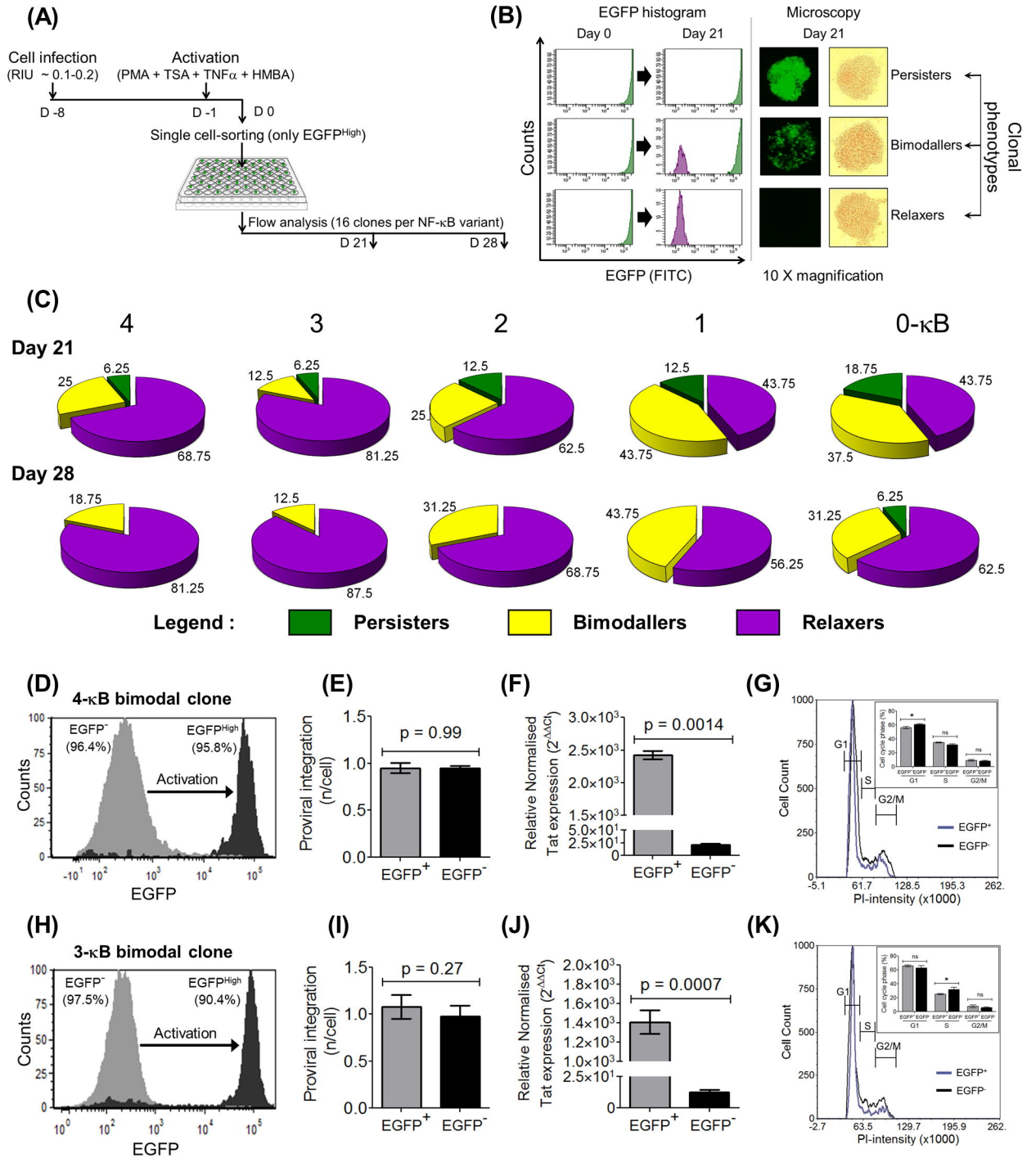
(A)
Cell infection
(RIU ~ 0.1-0.2)
Activation
(PMA + TSA + TNFα + HMBA)
D -8
D -1
D 0
Single cell-sorting (only EGFPHigh)
Flow analysis (16 clones per NF-κB variant)
D 21
D 28
(B)
EGFP histogram
Day 0
Day 21
Microscopy
Day 21
Counts
EGFP (FITC)
Persisters
Bimodallers
Relaxers
Clonal phenotypes
10 X magnification
(C)
4
3
2
1
0-κB
Day 21
25
6.25
68.75
12.5
6.25
81.25
12.5
25
62.5
12.5
43.75
43.75
18.75
43.75
37.5
Day 28
18.75
81.25
12.5
87.5
31.25
68.75
43.75
56.25
31.25
6.25
62.5
Legend :
Persisters
Bimodallers
Relaxers
(D)
4-κB bimodal clone
EGFP-
(96.4%)
EGFPHigh
(95.8%)
Activation
Counts
EGFP
(E)
Proviral integration (n/cell)
p = 0.99
EGFP+
EGFP-
(F)
Relative Normalised Tat expression (2-ΔΔCt)
p = 0.0014
EGFP+
EGFP-
(G)
Cell Count
G1
S
G2/M
EGFP+
EGFP-
PI-intensity (x1000)
Cell cycle phase (%)
ns
*
(H)
3-κB bimodal clone
EGFP-
(97.5%)
EGFPHigh
(90.4%)
Activation
Counts
EGFP
(I)
Proviral integration (n/cell)
p = 0.27
EGFP+
EGFP-
(J)
Relative Normalised Tat expression (2-ΔΔCt)
p = 0.0007
EGFP+
EGFP-
(K)
Cell Count
G1
S
G2/M
EGFP+
EGFP-
PI-intensity (x1000)
Cell cycle phase (%)
ns
*

Figure 6

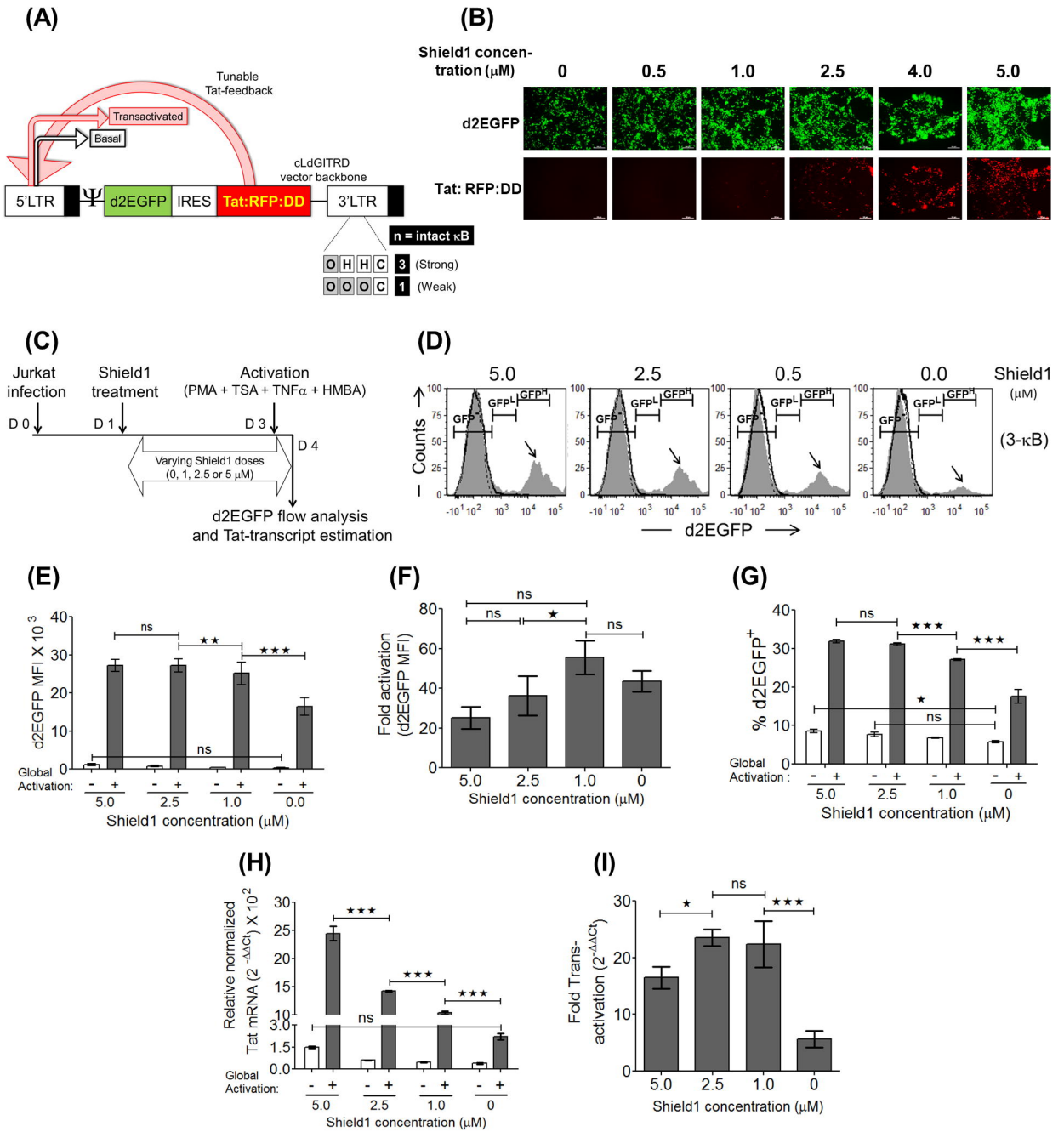
(A)
Tunable
Tat-feedback
Transactivated
Basal
cLdGITRD
vector backbone
5'LTR
Ψ
d2EGFP
IRES
Tat:RFP:DD
3'LTR
n = intact κB
O H H C 3 (Strong)
O O O C 1 (Weak)
(B)
Shield1 concen-
tration (μM)
0
0.5
1.0
2.5
4.0
5.0
d2EGFP
Tat: RFP:DD
(C)
Jurkat
infection
Shield1
treatment
Activation
(PMA + TSA + TNFα + HMBA)
D 0
D 1
D 3
D 4
Varying Shield1 doses
(0, 1, 2.5 or 5 μM)
d2EGFP flow analysis
and Tat-transcript estimation
(D)
5.0
2.5
0.5
0.0
Shield1
(μM)
(3-κB)
Counts
GFP-
GFPL
GFPH
d2EGFP
(E)
d2EGFP MFI X 10 3
ns
Global
Activation:
5.0
2.5
1.0
0.0
Shield1 concentration (μM)
(F)
Fold activation
(d2EGFP MFI)
ns
5.0
2.5
1.0
0
Shield1 concentration (μM)
(G)
% d2EGFP+
Global
Activation :
5.0
2.5
1.0
0
Shield1 concentration (μM)
(H)
Relative normalized
Tat mRNA (2 -ΔΔCt) X 10 2
Global
Activation:
5.0
2.5
1.0
0
Shield1 concentration (μM)
(I)
Fold Trans-
activation (2-ΔΔCt)
5.0
2.5
1.0
0
Shield1 concentration (μM)

Figure 7

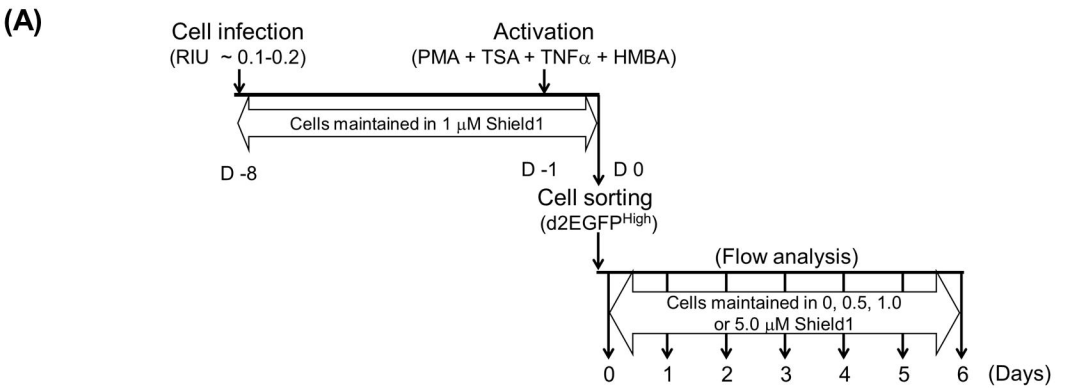
(A)
Cell infection
(RIU ~ 0.1-0.2)
Activation
(PMA + TSA + TNFα + HMBA)
Cells maintained in 1 μM Shield1
D -8
D -1
D 0
Cell sorting
(d2EGFP^High)
(Flow analysis)
Cells maintained in 0, 0.5, 1.0
or 5.0 μM Shield1
0 1 2 3 4 5 6 (Days)

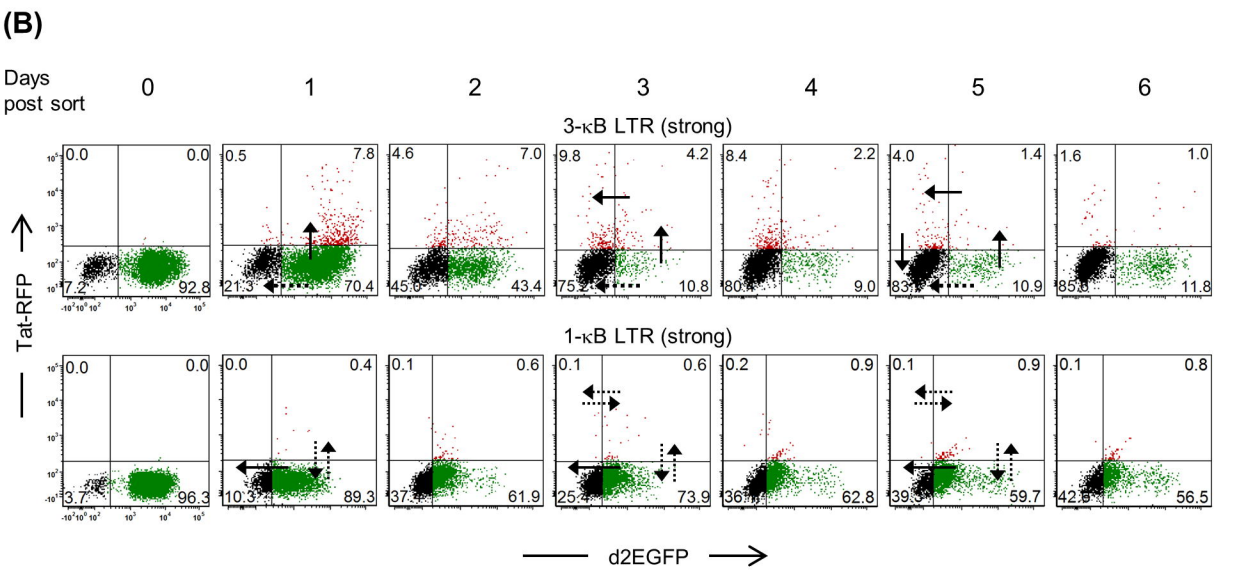
(B)
Days post sort
0 1 2 3 4 5 6
3-κB LTR (strong)
1-κB LTR (strong)
Tat-RFP
d2EGFP

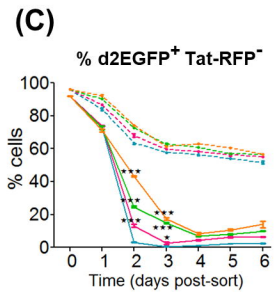
(C)
% d2EGFP+ Tat-RFP-
% cells
Time (days post-sort)

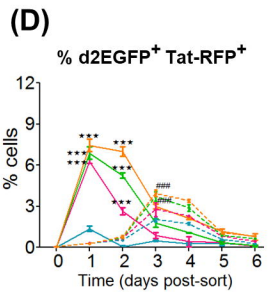
(D)
% d2EGFP+ Tat-RFP+
% cells
Time (days post-sort)

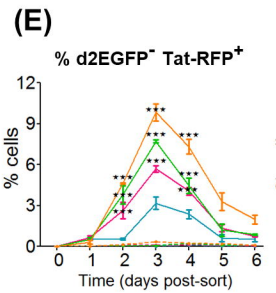
(E)
% d2EGFP- Tat-RFP+
% cells
Time (days post-sort)

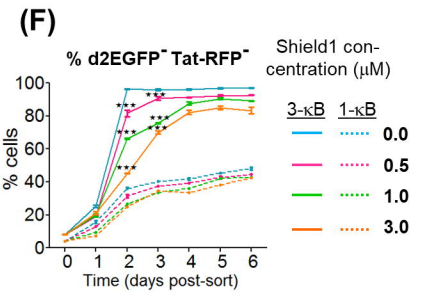
(F)
% d2EGFP- Tat-RFP-
% cells
Time (days post-sort)
Shield1 con-
centration (μM)
3-κB 1-κB
0.0
0.5
1.0
3.0

Figure 8

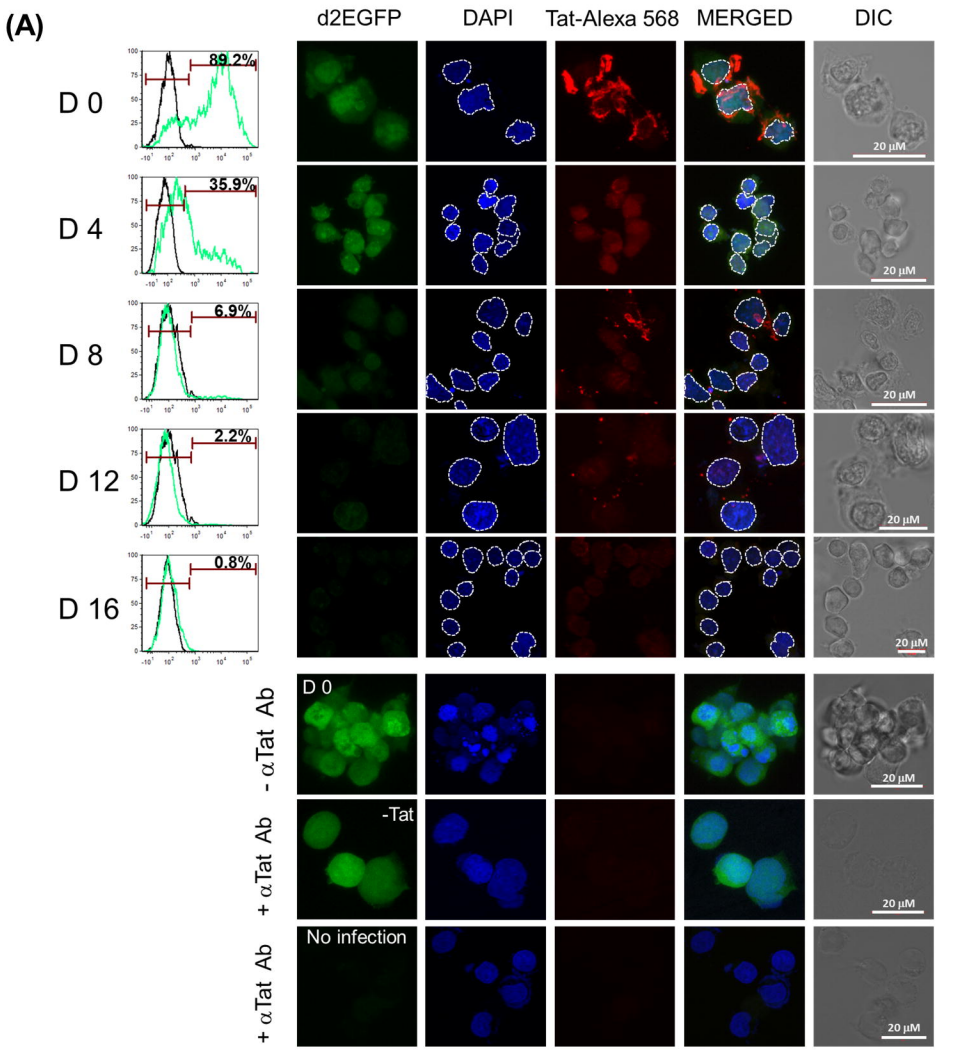
(A)
d2EGFP
DAPI
Tat-Alexa 568
MERGED
DIC
D 0
D 4
D 8
D 12
D 16
89.2%
35.9%
6.9%
2.2%
0.8%
20 µM
- αTat Ab
+ αTat Ab
+ αTat Ab
D 0
-Tat
No infection

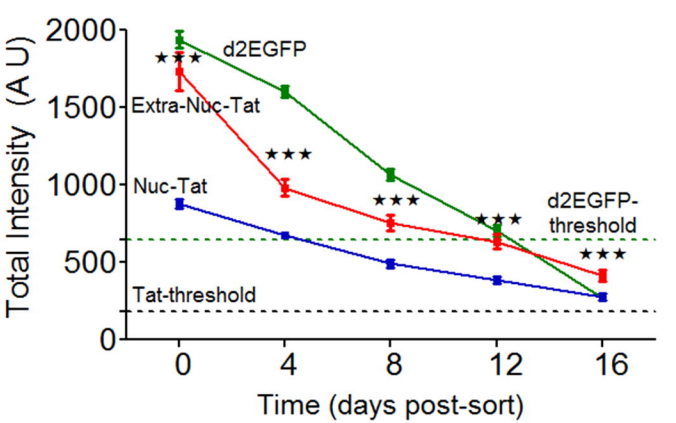
(B)
Total Intensity (A U)
2000
1500
1000
500
0
d2EGFP
Extra-Nuc-Tat
Nuc-Tat
d2EGFP-threshold
Tat-threshold
★★★
0
4
8
12
16
Time (days post-sort)

Figure 9

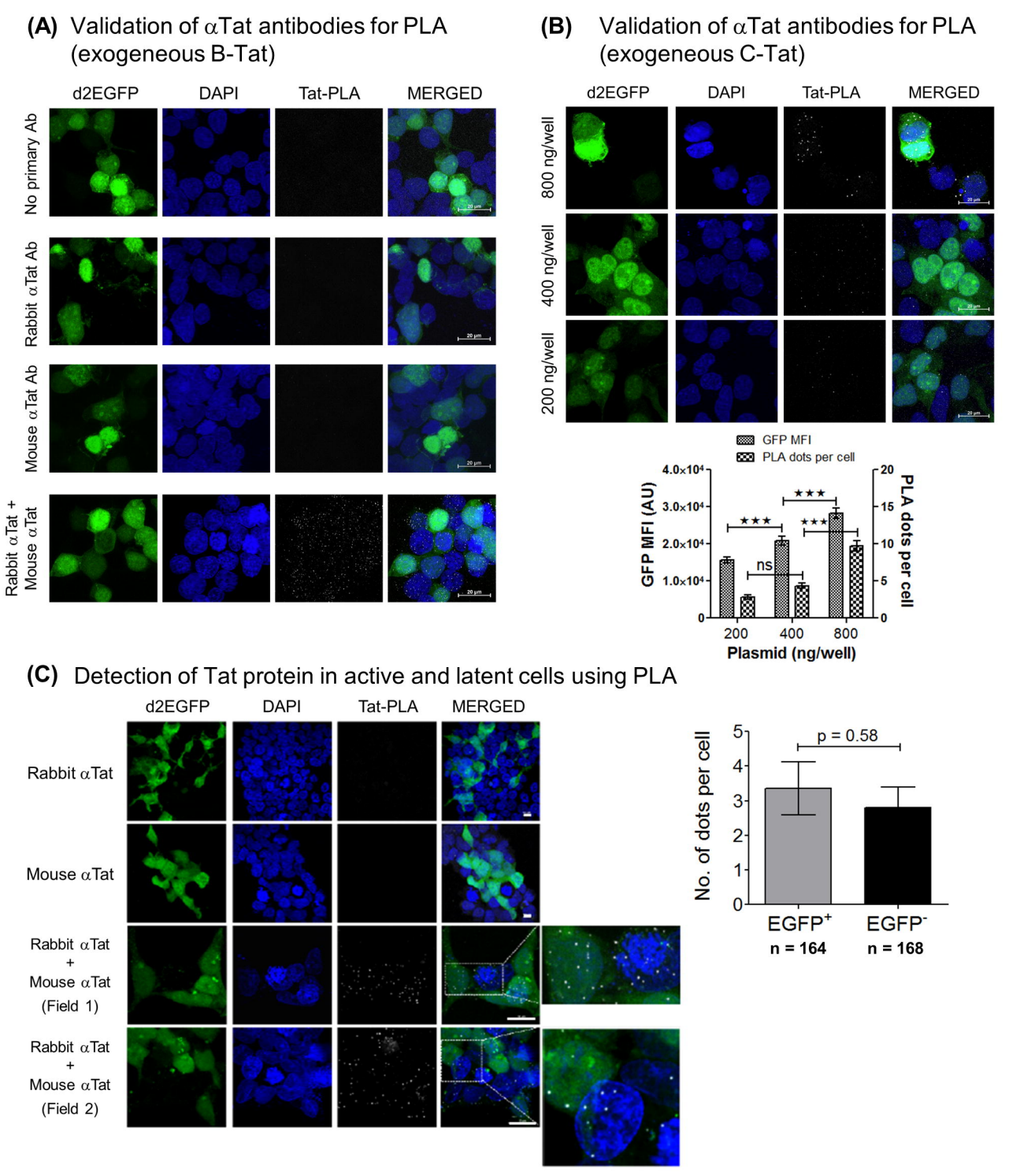
(A) Validation of αTat antibodies for PLA (exogeneous B-Tat)
d2EGFP
DAPI
Tat-PLA
MERGED
No primary Ab
Rabbit αTat Ab
Mouse αTat Ab
Rabbit αTat + Mouse αTat
(B) Validation of αTat antibodies for PLA (exogeneous C-Tat)
800 ng/well
400 ng/well
200 ng/well
GFP MFI
PLA dots per cell
GFP MFI (AU)
PLA dots per cell
Plasmid (ng/well)
ns
(C) Detection of Tat protein in active and latent cells using PLA
Rabbit αTat
Mouse αTat
Rabbit αTat + Mouse αTat (Field 1)
Rabbit αTat + Mouse αTat (Field 2)
No. of dots per cell
p = 0.58
EGFP+
EGFP-
n = 164
n = 168

Figure 10

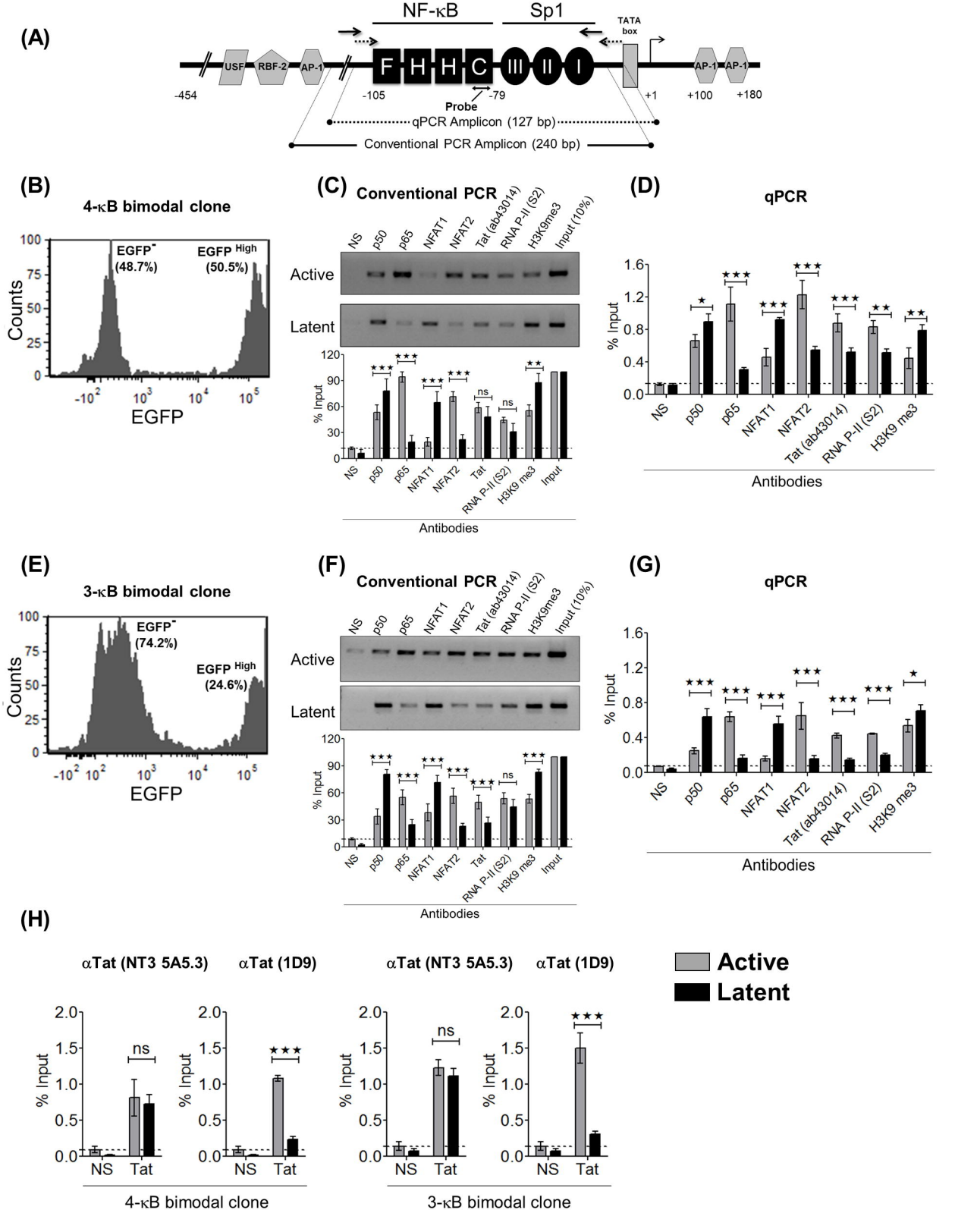
(A)
NF-κB
Sp1
TATA box
USF
RBF-2
AP-1
F H H C III II I
AP-1
AP-1
-454
-105
-79
Probe
+1
+100
+180
qPCR Amplicon (127 bp)
Conventional PCR Amplicon (240 bp)
(B)
4-κB bimodal clone
EGFP⁻ (48.7%)
EGFP High (50.5%)
Counts
EGFP
(C)
Conventional PCR
NS
p50
p65
NFAT1
NFAT2
Tat (ab43014)
RNA P-II (S2)
H3K9me3
Input (10%)
Active
Latent
% Input
Antibodies
(D)
qPCR
% Input
Antibodies
(E)
3-κB bimodal clone
EGFP⁻ (74.2%)
EGFP High (24.6%)
Counts
EGFP
(F)
Conventional PCR
Active
Latent
% Input
Antibodies
(G)
qPCR
% Input
Antibodies
(H)
αTat (NT3 5A5.3)
αTat (1D9)
αTat (NT3 5A5.3)
αTat (1D9)
Active
Latent
% Input
NS
Tat
4-κB bimodal clone
3-κB bimodal clone

Figure 11

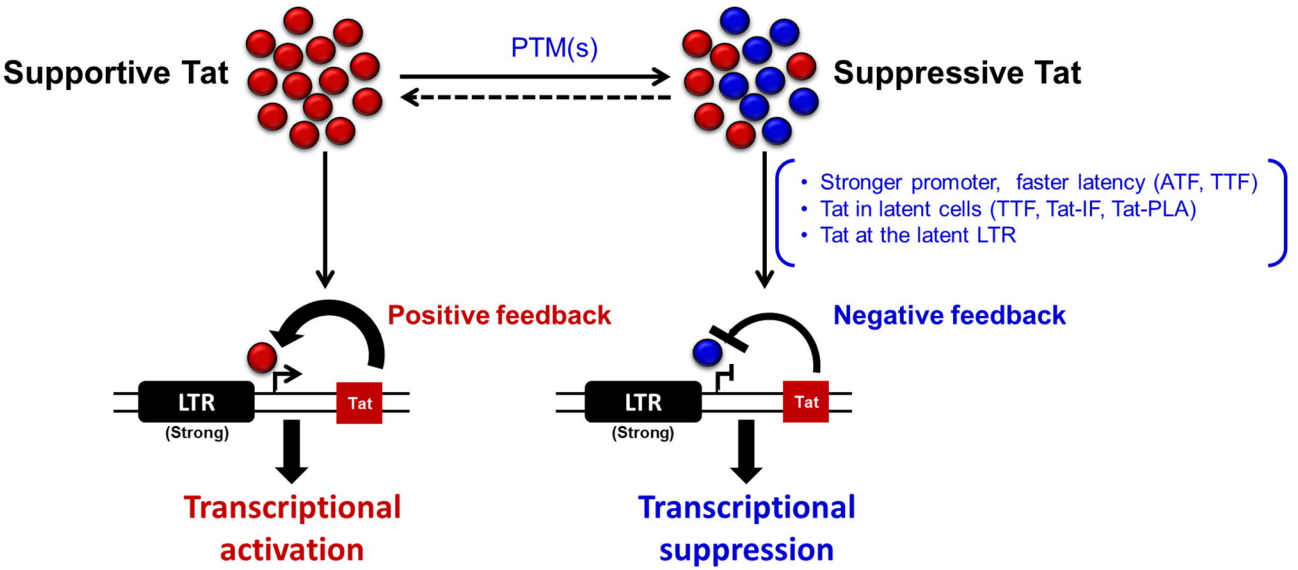
Supportive Tat
PTM(s)
Suppressive Tat
• Stronger promoter, faster latency (ATF, TTF)
• Tat in latent cells (TTF, Tat-IF, Tat-PLA)
• Tat at the latent LTR
Positive feedback
Negative feedback
LTR
(Strong)
Tat
LTR
(Strong)
Tat
Transcriptional activation
Transcriptional suppression